

**Zeitschrift:** Helvetica Physica Acta  
**Band:** 67 (1994)  
**Heft:** 7

**Vereinsnachrichten:** Réunion d'automne de la Société Suisse de Physique =  
Herbsttagung der Schweizerischen Physikalischen Gesellschaft =  
Autumn meeting of the Swiss Physical Society

**Autor:** [s.n.]

#### **Nutzungsbedingungen**

Die ETH-Bibliothek ist die Anbieterin der digitalisierten Zeitschriften auf E-Periodica. Sie besitzt keine Urheberrechte an den Zeitschriften und ist nicht verantwortlich für deren Inhalte. Die Rechte liegen in der Regel bei den Herausgebern beziehungsweise den externen Rechteinhabern. Das Veröffentlichen von Bildern in Print- und Online-Publikationen sowie auf Social Media-Kanälen oder Webseiten ist nur mit vorheriger Genehmigung der Rechteinhaber erlaubt. [Mehr erfahren](#)

#### **Conditions d'utilisation**

L'ETH Library est le fournisseur des revues numérisées. Elle ne détient aucun droit d'auteur sur les revues et n'est pas responsable de leur contenu. En règle générale, les droits sont détenus par les éditeurs ou les détenteurs de droits externes. La reproduction d'images dans des publications imprimées ou en ligne ainsi que sur des canaux de médias sociaux ou des sites web n'est autorisée qu'avec l'accord préalable des détenteurs des droits. [En savoir plus](#)

#### **Terms of use**

The ETH Library is the provider of the digitised journals. It does not own any copyrights to the journals and is not responsible for their content. The rights usually lie with the publishers or the external rights holders. Publishing images in print and online publications, as well as on social media channels or websites, is only permitted with the prior consent of the rights holders. [Find out more](#)

**Download PDF:** 15.01.2026

**ETH-Bibliothek Zürich, E-Periodica, <https://www.e-periodica.ch>**

Réunion d'Automne de la Société Suisse de  
Physique

Herbsttagung der Schweizerischen Physikalischen  
Gesellschaft

Autumn Meeting of the Swiss Physical Society

October 6, 1994

Aarau, Switzerland



## Nanosled Experiments: Determination of Dissipation and Cohesive Energies of C<sub>60</sub> with UHV-SFM

R. Lüthi, E. Meyer, H. Haefke, L. Howald, and H.-J. Güntherodt  
Institute of Physics, University of Basel, Klingelbergstr. 82, CH-4056 Basel, Switzerland

In this study we investigated the tribological properties of C<sub>60</sub> thin films which were deposited onto NaCl(001). The used scanning force microscope (SFM) allows simultaneous measurements of normal and lateral forces under ultrahigh vacuum (UHV) conditions. The friction coefficient at the interface between the probing tip (oxidized Si) and the C<sub>60</sub>-islands is found to be 0.15. By increasing the normal force from 2 to 10 nN, the lateral force on impact with the step edge is sufficient to move the C<sub>60</sub> island as an entity in a controlled way and without destroying them. From the analysis of the lateral force signals during the shear event, dissipation and cohesive energies of C<sub>60</sub> can be derived. The presented results have impact for the field of nanotechnology, e.g. as a nanosled-type transport system.

Due to their unique structure, fullerenes are expected to possess novel physical properties. Especially, their mechanical properties have attracted much attention by the scientific community[1]. The nearly spherical shape and low surface strength of fullerenes are believed to be the essential ingredients for a material that could play a role as important as PTFE (polytetrafluoroethylene).

In this study we investigated the tribological properties of C<sub>60</sub> on the mesoscopic scale with a scanning force microscope (SFM) allowing simultaneous measurements of normal and lateral forces under ultrahigh vacuum (UHV) conditions[2]. C<sub>60</sub> powder (purity 99.99 %, MER Corporation) was used as original material. The C<sub>60</sub> films were grown by vapor deposition onto NaCl(001) which was freshly cleaved in UHV. The substrate temperature was kept at room temperature.

The friction coefficient at the interface between the probing tip (oxidized Si) and the C<sub>60</sub>-islands is found to be 0.15.

Fig. 1a) and b) show two 530 × 530 nm<sup>2</sup> SFM images of C<sub>60</sub> islands grown on a NaCl(001) substrate. These gray scale images represent a top-view of the sample surface recorded at constant normal force. The height of the triangular or hexagonal shaped C<sub>60</sub> islands was determined to be 2 to 5 monolayers ( $\approx$  1.6-3.0 nm).

Normal forces between 1 and 2 nN (including adhesive forces) were applied between probing tip (oxidized Si) and sample. By increasing the normal force from 2 to 10 nN, the lateral force on impact with the step edge was sufficient to move the C<sub>60</sub> island as an entity in a controlled way and without destroying them (cf. Figs. 1a and b). Different modes of motion, such as translation and rotation could be performed by the controlled action of the probing tip.

From the analysis of the lateral force data (cf. Figs. 1c and 1d), first, the local friction coefficient [ $\mu=0.15 \pm 0.02$  for Si-tip (oxidized) vs. C<sub>60</sub> [4]] and, second, dissipation and cohesive energies of C<sub>60</sub> could be derived. An extremely small dissipation energy of about 0.25 meV per molecule and a cohesive energy of  $1.5 \pm 0.3$  eV was found. The corresponding shear strengths of 0.05 to 0.1 MPa are one order of magnitude smaller than typical values of

boundary lubricants, e.g. such as Langmuir-Blodgett films of Cd-arachidate[3]. A different behaviour was observed for the case of  $C_{60}$  on graphite: The  $C_{60}$  islands were disrupted and a collective motion of the islands could not be achieved.

$C_{60}$  islands might be used as a transport device for fabrication processes of nanometer-sized machines, whereby  $C_{60}$  islands might play the role of a transport carrier.

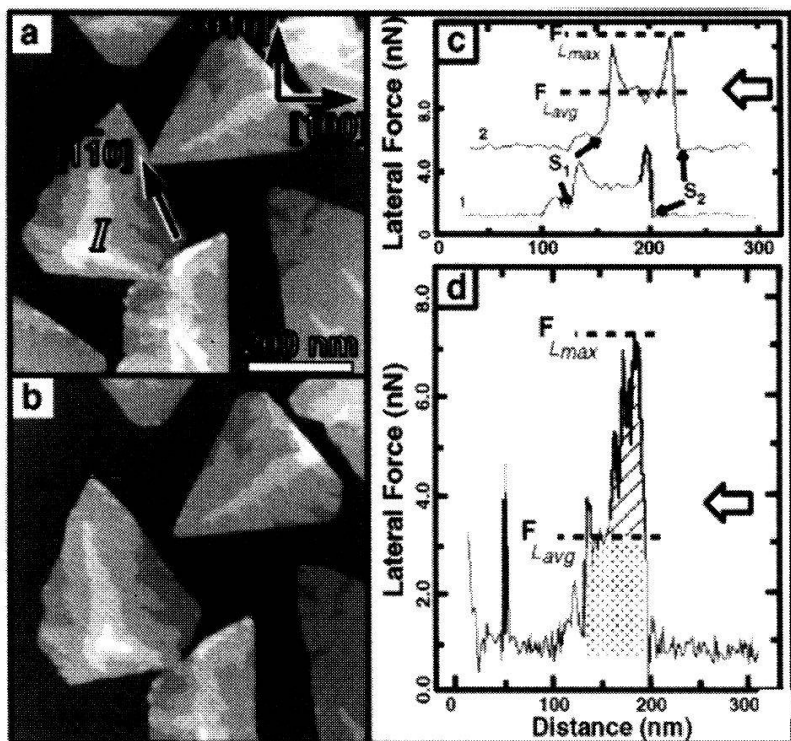


**Figure 1**

a-b: Sequence of  $530 \times 530 \text{ nm}^2$  top-view SFM images. The dark area corresponds to the  $\text{NaCl}(001)$  substrate whereas the bright areas are assigned to  $C_{60}$  islands. The crystallographic directions of the  $\text{NaCl}$  substrate are indicated top right in a. A  $C_{60}$  island (marked by I in Fig. 1a) was moved to the position shown in b by the controlled action of the probing tip and without destroying the island as an entity.

c-d: Lateral force signals of the shear event. Two representative snapshots of shear events of free  $C_{60}$  islands are shown in c (curve 2 is slightly offset). The shear event took place between the position  $S_1$  and  $S_2$ . The outlined arrow indicates the scan direction. The maximum lateral force  $F_{L_{max}}$  represents the amount of force necessary to overcome static friction of the  $C_{60}$  island on the  $\text{NaCl}$  substrate. During sliding (kinetic friction) the lateral force decreased to an average value  $F_{L_{avg}}$ .

d: The lateral force data of a fracture experiment, whereby the island I was separated from its neighbouring islands. The analysis of this curve yielded the cohesive (lined area) and dissipative energy (dotted area) of  $C_{60}$ .

## References

- [1] D. Tománek and M.A. Schlüter, *Phys. Rev. Lett.*, **67**, 2331 (1991).
- [2] L. Howald *et al.*, *J. Appl. Phys.* **63**, 117 (1993).
- [3] E. Meyer *et al.*, *Phys. Rev. Lett.* **69**, 1777 (1993).
- [4] R. Lüthi *et al.*, *Z. Phys. B* **95**, 1 (1994).

## Second-harmonic studies of pure DCANP and mixed DCANP/CdA LB Films at the air/water interface

L.M. Eng, M. Küpfer, Ch. Seuret, and P. Günter

Institute of Quantum Electronics, ETH Hönggerberg, CH-8093 Zürich

We report on novel investigations on non-linear optical DCANP (2-docosylamino-5-nitropyridin) Langmuir-Blodgett (LB) films by means of polarization, second harmonic (SH) and scanning force microscopy (SFM). Direct optical measurements at the air/water interface showed the molecules to reorient when depositing a LB film onto a solid substrate by the Langmuir-Blodgett method. Horizontal dipping (Langmuir-Schäfer method), however, resulted in the same surface structure being transferred onto the substrate as was found for the LB film floating on the water subphase.

Furthermore, the LB film was improved in film quality by adding 10-20% of Cadmium-arachidate (CdA) to the pure DCANP phase. This results in a surface structure free of defects as shown by SFM. Nevertheless, no significant changes in the optical properties of the mixed LB film were found.

For the application of non-linear optical materials in wave guides, filters and switches an essential prerequisite are the overall homogeneous and constant properties of the material in use. It is not only necessary that the non-linear optical material show a high hyperpolarization, but also that its physical structure is smooth on a scale much smaller than the typical wave length. Recently, we showed that scattering losses at defects of 10-100 nm in diameter significantly diminish the intensity of the propagating electromagnetic wave (~20 dB/cm) [1]. Thus, we are interested in improving these material quality for the assembling of a usable wave guide structure. In a *bottom-up* approach the construction of a perfect monomolecular layer is desired using LB molecules. Not only do these films offer a big variety for chromophore syntheses, but also can a wave guide structure be controlled on a molecular level.

Here, we investigated the effect of LB film transfer onto a solid substrate, a crucial problem with these type of molecular structures. The influence of asymmetric forces on the molecules can be seen in direct space thanks to our new set-up of SH and polarization microscopy [2].

Fig. 1 presents the DCANP monolayer film structure (a) when floating on the water subphase in our LB trough, (b) deposited onto a Pyrex substrate by perpendicular dipping (LB method), and (c) horizontally dipped by the Langmuir-Schäfer (LS) method. Please note that in the LS method the sample substrate slightly touches the floating LB molecules until they interact with the atoms at the sample surface. Therefore, the structure of the as-transferred LB film looks the same as for the floating monolayer (see Fig. 1a and 1c). In both cases, the DCANP film forms so-called spherulites of a mixed crystalline and amorphous structure [3].

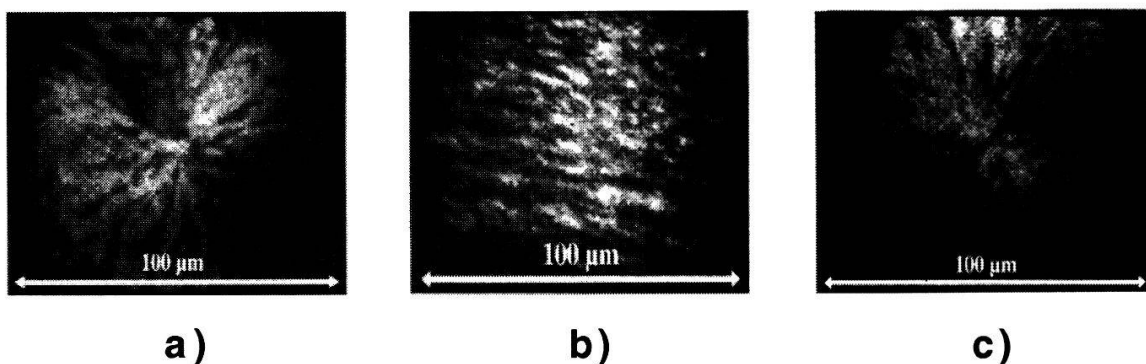


Fig. 1 : Domain structure of a DCANP LB film (a) floating on the water subphase, (b) deposited onto a Pyrex substrate by the LB method, and (c) horizontally dipped by the LS method.

Perpendicular dipping, however, results in preferential arrangement of the chromophore molecules along the dipping direction (Fig. 1b). This is due to the force gradient induced by capillary and meniscus forces at the water/substrate interface [3]. The non-linear optical anisotropy measured along and perpendicular to the dipping direction is 10:1.

The mechanical film properties of the DCANP LB film were recently improved by adding a known percentage of CdA to the DCANP phase [4]. Fig. 2 shows the behaviour of the non-linear optical susceptibility  $d_{33}$  as a

function of CdA concentration. As seen from this figure, the non-linear optical intensity is not affected too much for CdA concentrations below  $\sim 20\%$ . The film structure at this CdA concentration, however, shows a perfect monolayer smooth and free of defects over several hundred micrometers [4] as found in our recent SFM inspections. We therefore succeeded in optimizing a LB film with respect to its structure and transferring it onto a solid substrate.

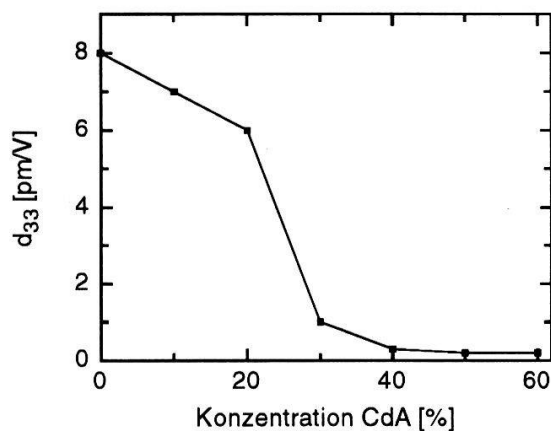


Fig. 2 : Non-linear optical susceptibility  $d_{33}$  of a mixed DCANP/CdA LB film as a function of CdA concentration.

## References :

- [1] Ch. Bosshard, et al., *Thin Solid Films*, **210/211** (1992) 198.
- [2] M. Flörsheimer, et al., *Ber. Bunsenges. Phys. Chem.*, **98** (1994) 521.
- [3] L. Eng, et al., *Second-harmonic studies of pure DCANP and DCANP/CdA mixtures at the air/water interface*, manuscript in preparation.
- [4] B. Schmidt, Diplomarbeit, ETH Hönggerberg (1993).

## Morphological changes during stretching of polypropylene films studied by scanning force microscopy

**S. Hild, W. Gutmannsbauer, R. Lüthi, H. Haefke, H.-J. Güntherodt**

Institute of Physics, University of Basel, CH-4056 Basel, Switzerland

A scanning force microscop (SFM) is used to characterize the surface structure of a row nucleated polypropylene film. With a home-build stretching machine for the available SFM morphological changes caused by stepwise stretching can be observed. The morphological changes during stretching the film are imaged. Stretching HEPP vertical to extrusion direction causes cracks advancing through several cristalline rows. Elongation parallel to extrusion direction, the separation of adjacent lamellae by a translatory displacement can be visualized.

The mechanical properties of crystalline polymers, like isotactic polypropylene, depend on its particular structural arrangement. The morphology varies with the conditions of crystallization. Crystallization which occurs in an extensional flow field, e. g. during the extrusion process, results in a row nucleated morphology. By a special combination of melt extrusion and annealing treatment, the row-nucleated structure is prepared as so called "hard elastic" morphology, where parallel aligned lamellar rows are connected to each other by extremly stable tie points [1,2]. The high uniaxial orientation of the row nucleated structure is related to the anisotropy of tensile behaviour. The special structure of hard elastic polypropylene (HEPP) films is responsible for its unique deformation behaviour.

Up to now, the morphology of polymer films and deformation induced morphological changes have been investigated by X-ray diffraction and transmission electron microscopy (TEM). For surface analysis by TEM, polymers need a special sample preparation, e.g., metallization, which can alter the surface. Because of the sample preparation it is not possible to investigate more than one deformation state per sample. The method of scanning force microscopy (SFM) allows to examine surfaces of polymers without any sample preparation [3,4].

For our studies we used a commercial available HEPP film [5]. The SFM was performed under ambient conditions and by operating the force microscope in the constant force mode. In order to investigate the changes in HEPP morphology as a function of "stretch" a small stretching machine (SM) was constructed. This novel SM allows a stepwise stretching up to 100% extension.

Crystalline and amorphous regions of the unstrained HEPP film were imaged (Fig. 1). The crystalline regions have a thickness of 20 nm and lateral extention from 25 nm to 100 nm. The width of the intercrystalline regions are 10 nm. Stretching of HEPP vertical to the lamellar rows causes vertical cracks advancing through several cristalline rows (Fig. 2a). Brittle fracture at an elongation of about 15% occurs. Elongation parallel to the lamellar

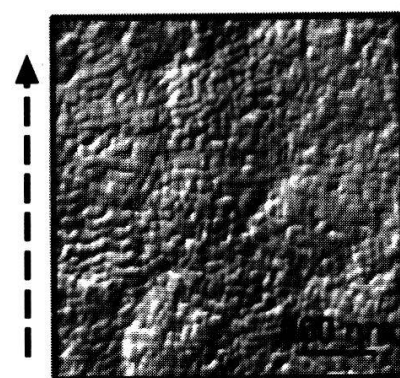
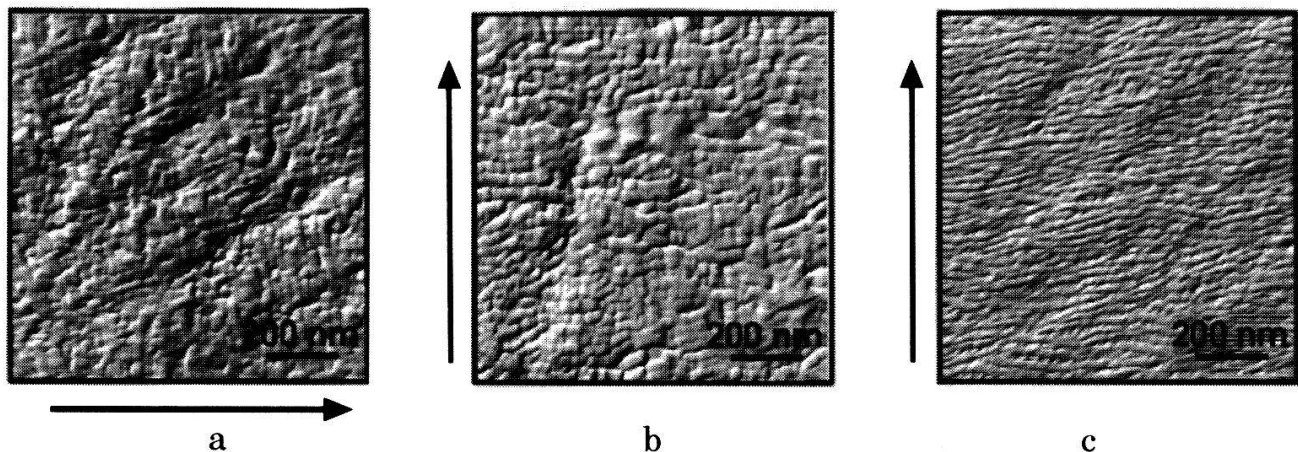


Fig.1: SFM image of an unstrained HEPP film. Arrow indicates the orientation direction.

rows, elongation rates up to 350% are possible. The deformation mechanism for parallel stretching is generally described by the separation of adjacent lamellae under tensile load and the building of voids [1,2]. Elongation rates up to 10% lead to the perfection of lamellar alignment by their non disruptive tilting (Fig. 3b). At higher elongation rates adjacent lamellae are separated by translatory displacement and tie molecules are pulled out (Fig. 3c). The distance between adjacent tie molecules vary between 25 nm and 100 nm which is in the same range as the lateral lamellar



**Fig.2:** SPM image of the strained HEPP film. Arrow indicates the stretching direction. (a) by 10% vertical extension (b) by 10% parallel extension (c) by 100% parallel extension

extension. Because of this, the tie molecules should be microfibrils generated during the extrusion process.

The SPM images shows that the macroscopic increase in sample length is caused by the orientation of noncrystalline molecules and the enlargement of voids the translatory lamellar displacement. The microscopic elongation can be described by a two-phase model proposed by Noether et al [2]: Depending on the elongation  $\epsilon$  of the film the extended lamellar size  $l_e$  can be calculated by

$$l_e = l_u (1 + \epsilon) \quad (1)$$

with the lamellar unit  $l_u = a + c$ , whereas  $a$  is the interlamellar and  $c$  the crystalline size [2]. From known dimensions of unstrained crystalline and noncrystalline regions the microscopic increase in length can be calculated for a given elongation with equitation (1). The stretching induced increase in noncrystalline width and the crystalline thickness for these elongation rates are also determined by SPM. The thickness of the elongated lamellar units is given by addition of the thickness of crystalline and noncrystalline regions. The microscopic elongation is calculated in relation to the nonstrained dimensions. Comparing the macroscopic and the microscopic strain, a good correspondence for elongation rates smaller than 100% was found. The increase in interlamellar space for a film extend by 100% is smaller than expected from macroscopic extensions. A possible explanation is given by the limitation the void enlargement by the flexibility of the microfibrils connecting the lamellae.

## References:

1. M. Miles, J. Petermann, H. Gleiter, J. Macromol. Sci., B12 (4) 523 (1976)
2. H. D. Noether, W. Whitney, Kolloid-Z.U.Z. Polym. 251 991 (1973)
3. R. M. Overney, R. Lüthi, H. Haefke, E. Meyer, H. J. Güntherodt, S. Hild, J. Fuhrmann, Appl. Surf. Sci. 64, 197 (1993).
4. R. M. Overney, H.-J. Güntherodt, S. Hild; J. Appl. Phys. 75(3) 1401 1994
5. Celgard 2500, Hoechst Celanese Corporation, Charlotte, NC, USA

## Magnetic Properties of Nanosized Wires

J. Meier, A. Blondel, B. Doudin, J.-Ph. Ansermet

Institut de Physique Expérimentale, EPFL, 1015 Lausanne, Switzerland

Template synthesis of nanosized wires by electrodeposition in polycarbonate track-etched membranes has been successfully used for Ni, Co and (NiFe). An assembly of wires with preferred orientation gives a model for magnetism of infinite cylinders. The variation of the coercive field with diameter and temperature is interpreted in terms of a non uniform magnetization reversal and a large magnetoelastic contribution.

Commercially available nanoporous track-etched polycarbonate membranes [1] were coated with gold on one side. This side served as a cathode in an electroplating solution of either Ni-Sulfate [2] or Ni- and Fe-Sulfate [3]. Applying a constant voltage to this electrolytical cell allowed a controlled deposition of Ni or (NiFe) in the pores. For TEM observations the polycarbonate matrix was dissolved. A small diameter distribution was found [2]. The permalloy composition was determined by EDS to be  $\text{Ni}_{80\pm 5}\text{Fe}_{20\pm 5}$ .

Hence our samples consisted of assemblies of parallel nanowires with a length of 6-10  $\mu\text{m}$  and a range of mean diameters  $d$  of 30-300 nm. As expected, hysteresis loops showed a large magnetic anisotropy perpendicular to the membrane, i.e. parallel to the wires. Choosing a larger mean pore diameter  $d$  of the membrane results in a lower coercive field  $H_c$  (Fig.1). This is in contrast to the case of a uniform reversal of the magnetization [4] in which  $H_c$  is independent of  $d$ .

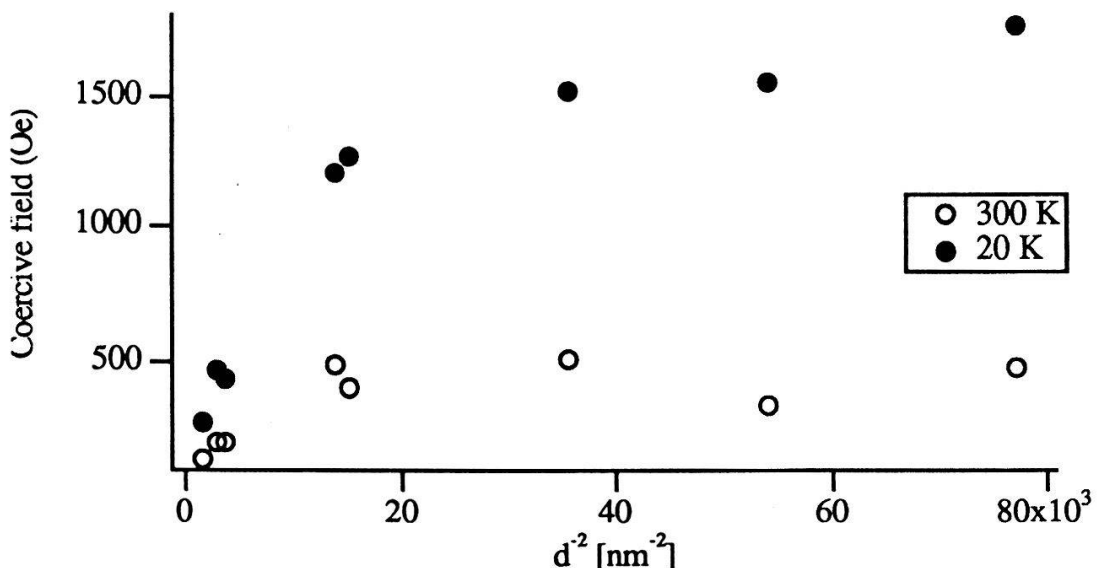


Fig.1: Coercive field of Ni wires of average diameter  $d$  at two temperatures. The line corresponds to the data used to fit to the curling model described in the text.

At low temperature and for small diameters we find a behaviour consistent with the curling mode [5]. For an infinite cylinder, the coercive field  $H_c$  is given by:

$$H_c = \frac{2K_0}{M_s} + 2.16\pi \frac{M_s}{S^2}$$

where  $S = \frac{d}{2M_s \sqrt{A}}$ ,  $K_0$  is the anisotropy constant and  $A$  is the exchange constant.

We deduced a value of  $A = 6 \cdot 10^{-12}$  J/m corresponding to the reported value  $1.1 \cdot 10^{-11}$  J/m found in a similar way for Fe [6]. The extrapolation to large diameters yields a coercive field of 1200 Oe corresponding to an anisotropy constant of  $3 \cdot 10^4$  J/p0m<sup>3</sup>.

For the simplest models of magnetization reversal, one expects a temperature dependence of  $H_c$  of the following form [7]:

$$H_c(T) = H_c(0) \left(1 - \sqrt{\frac{T}{T_B}}\right)$$

where  $T_B$  is the blocking temperature above which superparamagnetic behaviour occurs. In our samples we found a linear decrease of  $H_c$  with  $T$ , for the case of the applied field aligned with the wires as well as for the applied field perpendicular to the wires. Then we dissolved the polycarbonate matrix. The "free" wires of this sample were measured perpendicular to the applied field. The temperature dependence of  $H_c$  of this sample was strongly reduced. A (NiFe) sample, of which the linear magnetostriction coefficient  $\lambda_s$  is known to be very small, showed no temperature dependence of  $H_c$  (Fig. 2). These experiments strongly support the hypothesis of a considerable contribution of the magnetoelastic energy to the total anisotropy energy with stresses induced by the thermal expansion of the plastic matrix.

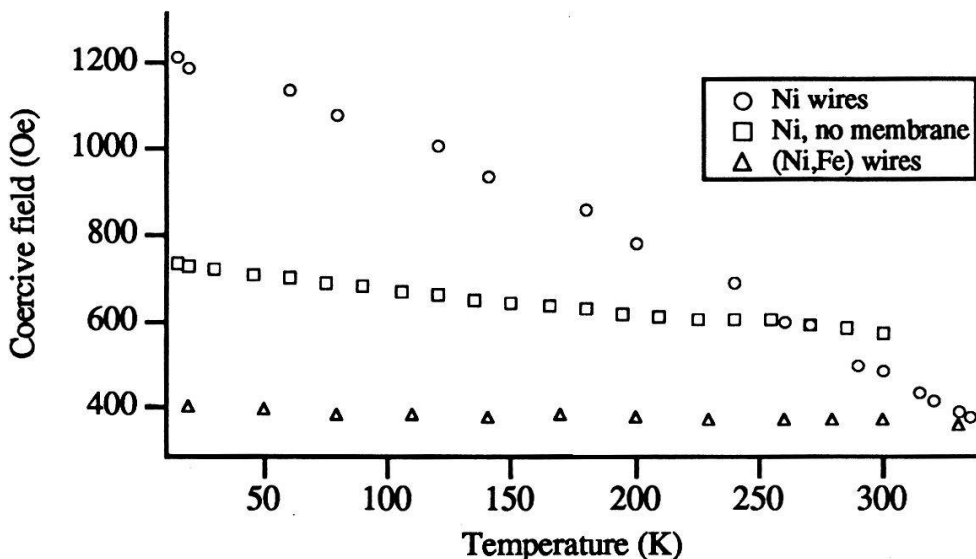


Fig.2: Coercive field vs. temperature for wires with an average diameter of about 80nm.

## References

- [1] R.L. Fleisher, P.B. Price and R.M. Walker, in *Nuclear tracks in solids*, Univ. of California Press (Berkeley, 1975)
- [2] I. Chlebny, B. Doudin and J.-Ph. Ansermet, *Nanostructured Mater.* **2**, 637 (1993)
- [3] J.M. Brownlow, *J. Appl. Phys.* **38**(3), (1967)
- [4] E.C. Stoner and E.P. Wohlfarth, *Phil. Trans. Roy. Soc. London A* **240**, 599 (1948)
- [5] E.H. Frei, S. Shtrikman and D. Treves, *Phys. Rev.* **106**, 446 (1957)
- [6] G.T.A. Huysmans, J.C. Lodder and J. Wakui, *J. Appl. Phys.* **64**(4), 2016, (1988)
- [7] E.F. Kneller and F.E. Luborsky, *J. Appl. Phys.* **34**(3), 656, (1963)

# Atom and Electron Motions on the Si(001) Surface Generated by First Principles Molecular Dynamics

E.P. Stoll<sup>1,3</sup>, A. Baratoff<sup>2</sup>, A. Mangili<sup>3</sup>, and D. Maric<sup>3</sup>

<sup>1</sup>Physik-Institut, Universität Zürich-Irchel, Winterthurerstr. 190, CH - 8057 Zürich,

<sup>2</sup>Institut für Physik, Universität Basel, Klingelbergstr. 82, 4056 Basel, <sup>3</sup>Centro Svizzero di Calcolo Scientifico, Via Cantonale, 6928 Manno

The time evolution of the atomic positions and of the electronic densities of the highest occupied states on the Si(001) surface are investigated by first-principles molecular dynamics. The most important changes accompanying the anharmonic flipping of dimers confirm the experimental facts that at room temperature the dimers in the top layer of the Si(001) surface appear symmetric in STM topographic images, whereas at low temperatures ( $T \leq 120$  K) dimers appear tilted.

Over the past years controversy has continued over arrangement of Si atoms on its (001) surface at room temperatures. Whereas scanning tunneling microscopy (STM) images of occupied states [1] mostly show symmetric dimers, angular-resolved UV [2] and X-ray photoemission [3] spectra are essentially like at low temperatures where a transition to an ordered  $c(4 \times 2)$  consisting of antiferrodistortive-ordered Si-dimers has been observed in LEED [4]. Following Chadi's prediction of this structure [5], and related work on surface phonons [6] a similar controversy arose between ground state computations, even at the ab-initio level. Thus different pseudopotential calculations predicted either that the symmetric  $(2 \times 1)$  [7] or that the antiferrodistortive  $c(4 \times 2)$  arrangement [8] of tilted Si-dimers should be stable. The issue was settled in favor of the latter; the energy difference with respect to the symmetric (saddle point) configuration is only 0.09 eV per dimer [9], however. In the meantime scanning tunneling microscopes have steadily improved and at low temperatures rather large domains showing asymmetric dimers with the expected  $c(4 \times 2)$  arrangement have been imaged [10]. Nevertheless a transition is expected from this low temperature  $c(4 \times 2)$  ordered phase to a disordered  $(2 \times 1)$  phase above a transition temperature estimated between 200 [4] and 120 K [10].

The small energy barrier has important implications. First the symmetric appearance of dimers in STM topographs at room temperature could indeed be due to time averaging over thermally activated flips between degenerate stable configurations tilted in opposite directions [1]. Next, simulations based on approximate theoretical models can easily incorrectly predict the flip rate or even the qualitative dimer dynamics [11]. We therefore embarked on a first-principles molecular dynamics investigation of the type pioneered by Car and Parrinello [12]. Finally, the probing tip of STM can itself cause the nearest dimer to flip as it is scanned over [1], as illustrated in a very recent Car-Parrinello-like calculation [13]. Our investigation at the free Si(001) surface is worthwhile in its own right as it reveals for the first time the coupled evolution of Si nuclei and electronic states localized in the top layers.

Since dimers form rows and are primarily coupled along the  $[\bar{1}10]$  direction, we consider a  $2 \times 4$  surface cell containing four dimers above three free layers each containing eight Si atoms, followed by five fixed layers with the bulk [001] spacing. The bottom layer was saturated with pairs of hydrogen atoms. We use the same pseudopotentials and cutoff (8Ry) as in a previous successful study of the Si(111)  $2 \times 1$  reconstruction [14]. Plane waves with  $k=0$  were deemed sufficient. Their coefficients were initially optimized for the symmetric configuration of [7] and the ionic positions were then relaxed simultaneously. The resulting arrangement consists of dimers alternately tilted by  $\sim 0.53 \text{ \AA}$  forming a  $p(2 \times 2)$  configuration known to be almost degenerate with  $c(4 \times 2)$  [5-8]. The system was then gradually heated to 1000 K via rescaling of the velocities, cooled, and finally kept at 300 K over  $\sim 45\,000$  time steps (5.5 ps in real time). In two independent runs dimers executed irregular oscillations with a mean period of 0.3 ps about tilted configurations and flipped on a comparable time scale every 1.5 ps on the average.

Upon averaging the electron density of the highest occupied states over a time interval sufficient for dimers to flip from one tilted configuration into the other, surfaces of low constant density ( $\sim 0.015 \text{ e}/\text{\AA}^3$ ) acquire a symmetrical appearance much like STM images measured at room temperature [1]. On the other hand, averaging over intervals short enough that each dimer oscillates only about one tilted position yields equidensity surfaces similar to STM images measured at low temperatures [10].

We thank W. Andreoni, I.P. Batra, R. Car, S. Ciraci, G. Galli, J. Hutter and M. Parrinello for helpful discussions and technical support. Part of the work and a large amount of the calculations have been performed at the IBM Research Division, Zurich Research Laboratory.

## References

- [1] R.J. Hamers, R.M. Tromp, and J.E. Demuth, Phys. Rev. **B34**, 5343 (1986).
- [2] L.S.O. Johansson, R.I.G. Uhrberg, P. Mårtensson, and G.V. Hansson, Phys. Rev. **B42**, 1305 (1990).
- [3] E. Landemark, C.J. Karlsson, Y.-C. Chao, and R.I.G. Uhrberg, Phys. Rev. Lett. **69**, 1588 (1992).
- [4] T. Tabata, T. Aruga and Y. Murata, Surf. Sci. **179**, L63 (1987).
- [5] D.J. Chadi, Phys. Rev. Lett. **43**, 43 (1979).
- [6] O.L. Alerhand and E.J. Mele, Phys. Rev. **B35**, 5533 (1987).
- [7] I.P. Batra, Phys. Rev. **B41**, 5048 (1990).
- [8] Z. Zhu, N. Shima, and M. Tsukada, Phys. Rev. **B40**, 11868 (1989).
- [9] J. Dabrowski and M. Scheffler, Appl. Surf. Sci. **56-58**, 15 (1992).
- [10] R.A. Wolkow, Phys. Rev. Lett. **68**, 2636 (1992); G. Meyer, (private communication).
- [11] J. Gryko and R.E. Allen, Ultramicroscopy **42 - 44**, 793 (1992).
- [12] R. Car and M. Parrinello, Phys. Rev. Lett. **55**, 2471 (1985); G. Galli and M. Parrinello, *Ab-initio Molecular Dynamics: Principles and Practical Implementation*, NATO ASI Series, Kluwer, **E205**, 283 (1991).
- [13] K. Cho and J.D. Joannopoulos, Phys. Rev. Lett. **71**, 1387 (1993).
- [14] F. Ancilotto, W. Andreoni, A. Selloni, R. Car, and M. Parrinello, Phys. Rev. Lett. **65**, 3148 (1990).

## Etude de microréseaux supraconducteurs

C. Ammann

Institute of Theoretical Physics, University of Lausanne, CH-1015 Lausanne

Nous appliquons la théorie de Ginzburg-Landau (G-L) à des réseaux mésoscopiques bidimensionnels de fils supraconducteurs dans un champ magnétique uniforme transverse au plan des fils. Pour un microréseau particulier appelé Pont de Wheatstone, nous établissons la courbe de transition de phase normale-supraconductrice dans l'espace de phase température-flux magnétique, nous explorons numériquement le comportement du paramètre d'ordre dans la zone supraconductrice, puis nous représentons le gain d'énergie de Gibbs et la valeur du supercourant en fonction du flux pour des températures données.

Un microréseau supraconducteur est un arrangement bidimensionnel de fils de diamètre négligeable en regard de la longueur de cohérence  $\xi(T)$  du matériau supraconducteur qui les compose. La dimension caractéristique des structures ainsi formée est de l'ordre de  $\xi(T)$ . Perpendiculairement au plan des fils, un champ magnétique uniforme est appliqué, induisant dans les fils des supercourants dont il s'agit de calculer le sens et l'intensité.

Pour ces structures inhomogènes, la théorie G-L est la plus appropriée. Elle postule la forme suivante du gain d'énergie de Gibbs

$$\Delta G(\varphi, A) = \xi^3 \int d^3x \left\{ \frac{|\alpha|^2}{\beta} (|\hat{p}\varphi|^2 - |\varphi|^2 + \frac{1}{2}|\varphi|^4) + \frac{\mu_0}{2} H_{\text{ind}}^2 \right\}, \quad (1)$$

où  $x = \tilde{x}/\xi(T)$  est le vecteur position normalisé, avec  $\tilde{x}$  le vecteur position effectif;  $\alpha \propto (T - T_c)$  et  $\beta$  sont les deux paramètres usuels de la théorie G-L ; le paramètre d'ordre G-L normalisé  $\varphi$  est défini par  $\varphi(x) = \tilde{\varphi}(x)/\varphi_\infty$ , avec  $\tilde{\varphi}$  le paramètre d'ordre effectif et  $\varphi_\infty^2 = |\alpha|/\beta$ ;  $H_{\text{ind}}(x)$  est le champ magnétique induit par les supercourants dans le microréseau;  $\hat{p}$  est l'opérateur d'impulsion invariant de jauge défini par  $\hat{p} = -i\nabla_x - A$ , où  $A = (2\pi/\Phi_0)\tilde{A}$ , avec  $\Phi_0$  le quantum de flux et  $\tilde{A}$  un potentiel vecteur.

L'énergie de Gibbs est minimisée si le paramètre d'ordre satisfait l'équation suivante

$$\hat{p}^2\varphi - \varphi + |\varphi|^2\varphi = 0, \quad (2)$$

et si la densité de supercourant vaut  $J^p = -m\xi J/(e|\varphi_\infty|^2\hbar)$ , où  $J = \Re(\varphi^*\hat{p}\varphi)$ , est la densité normalisée de supercourant.  $m$  et  $e$  sont la masse et la charge de l'électron.

Dans le cas unidimensionnel d'un fil extrêmement fin, la solution exacte de l'équation non-linéaire (2) est formée de combinaisons de fonctions elliptiques et dépend de deux paramètres  $J$  et  $N_0$ , qui est la valeur extrême de  $|\varphi|^2$  dans le fil.

Pour un microréseau particulier, la solution spécifique à la géométrie est déterminée par les conditions aux noeuds qui traduisent la façon dont les paramètres d'ordre s'y rejoignent. Les jonctions étant homogènes, les conditions sont les suivantes :

1. le paramètre d'ordre doit être continu aux noeuds,
2. la somme des supercourants doit s'annuler aux noeuds (loi de Kirchhoff),
3. la somme des dérivées de  $|\varphi|^2$  doit s'annuler aux noeuds.

Le Pont de Wheatstone [1] étudié ici (Fig. 1), est caractérisé par deux paramètres : la demi-longueur de la branche centrale  $l(\xi(T))$  et le rapport entre la longueur des branches latérales et de la branche centrale  $K$ . La figure 1 représente ce microréseau pour  $K = 3$ . La transition de phase supraconductrice-normale est de deuxième ordre. Ainsi nous utilisons l'équation (2) linéarisée, combinée avec les conditions aux noeuds, pour obtenir les courbes  $l(T)$  en fonction du flux magnétique dans une des boucles  $\Phi$ , pour lesquelles  $|\varphi|$  est nul (Fig. 2). La solution de température la plus élevée (en gras sur la figure 2) correspond à la courbe de transition de phase dans l'espace  $\{l(T), \Phi\}$ . Cette courbe est périodique de période  $\Phi_0$ . Seules deux types de configurations du paramètre d'ordre sont réalisées : soit les paramètres d'ordre sont égaux aux noeuds ((a) dans les figures), soit ils sont déphasés de  $\pi$  ((b) dans les figures). Pour ces deux types de configurations, le paramètre d'ordre est égal dans les deux branches latérales et  $J = 0$  dans la branche centrale.

La résolution numérique a été effectuée dans le cas  $K = 3$  pour différentes températures. Le supercourant, qui est alors d'écrantage (i.e. circulant exclusivement dans les branches latérales), et le gain d'énergie de Gibbs sont représentés en fonction du flux pour les configurations (a) et (b) dans le cas où  $l(T) = 0.5$  (Fig. 3). Ces fonctions sont également de période  $\Phi_0$ . Ces calculs presupposent que le diamètre des fils est négligeable. Dans cette approximation, on voit qu'il existe dans la zone supraconductrice une transition de premier ordre entre les configurations (a) et (b).

Les microréseaux supraconducteurs ont un avenir certain dans l'électronique. Même sans jonctions Josephson, certaines géométries peuvent avantageusement tenir lieu de SQUID [2]. Par ailleurs, de nouvelles techniques expérimentales [3] permettent de confronter les résultats théoriques avec ceux obtenus par l'expérimentation directe.

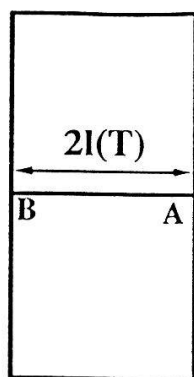
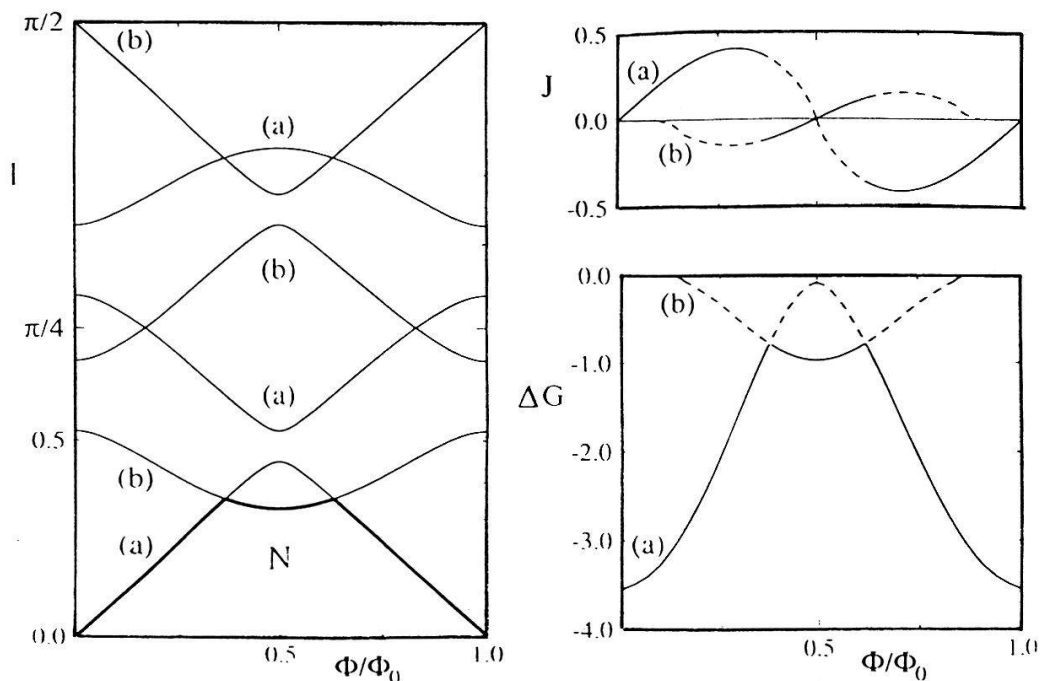


Fig. 1 ↑

Fig. 2 →

Fig. 3 →→



### Références

- [1] H. J. Fink, Phys. Rev. B **45**, 4799 (1992).
- [2] H. J. Fink, V. Grünfeld and A. López, Phys. Rev. B **35**, 35 (1987).
- [3] K. Runge and B. Pannetier, Europhys. Letter **24** (9), 737 (1993).

# Transmission through one-dimensional periodic media

Emilia Liviotti

*Institut de Physique Théorique, Université de Lausanne  
CH-1005 Lausanne, Switzerland*

The transmission through a one-dimensional periodic system is studied, using the transfer matrix method. The connection of the transmission coefficient with the Chebyshev polynomials of the second kind is shown, emphasizing that this result is valid only for particular ranges of values of the wave number. The position and the width of these Chebyshev-ranges are independent from the number of periods. The conditions for perfect transmission, which are related to the roots of these polynomials, have been analysed. These results may be applied to electromagnetic wave propagation in dielectric films, to electron scattering in quantum wells and to phonon transmission in superlattices.

Wave propagation in low-dimensional solids forms the basis for current advances in microstructure technology and for detailed analysis of wave interference effects in mesoscopic structures. Especially, one-dimensional systems are very useful for both theoretical and experimental studies. It is possible to give an uniform description of the transmission through a one-dimensional periodic system, making use of the transfer matrix method. The basic idea is to describe the propagation of a generic wave in a medium, replacing the wave equation by an appropriate matrix. Let us consider a single box, which can be a region of the space where there is a certain potential barrier, a semiconductor or a dielectric layer. We suppose that a unit amplitude wave incident from the left is transmitted through the box to the right. If we call  $M$  the transfer matrix through the potential and  $D$  the matrix which describes the propagation in the empty space between two following potentials[1, 2], then the total transfer matrix  $M(N)$  for the periodic system with  $N$  periods is given by:

$$M(N) = M \cdot D \cdot M \cdot D \cdots = M \cdot (D \cdot M)^{N-1}. \quad (1)$$

Using the unimodular property, which is a consequence of the current conservation, of the  $(D \cdot M)$  matrix [3, 4], the modulus of the transmission coefficient for  $N$  periods can be written in a compact way:

$$|t_N|^2 = \left(1 + \left|\frac{r_N}{t_N}\right|^2\right)^{-1} = \left(1 + \left|\frac{r}{t}\right|^2 P_{N-1}^2(z)\right)^{-1} \quad (2)$$

where  $z(k) = \frac{1}{2}Tr(D \cdot M)$  and  $r$  and  $t$  are the reflection and transmission coefficients of the single potential. The function  $P_N(z)$  is:

$$P_N(z) = \begin{cases} \sin[(N+1)\phi]/\sin(\phi) & |z| < 1, z = \cos \phi \\ \sinh[(N+1)\varphi]/\sinh(\varphi) & z > 1, z = \cosh \varphi \\ (-)^N \sinh[(N+1)\varphi]/\sinh(\varphi) & z < -1, z = -\cosh \varphi. \end{cases} \quad (3)$$

When  $|z| < 1$  we recognize in  $P_N(z)$  the Chebyshev polynomial of the second kind  $U_N(z)$  of degree  $N$  [5, 6, 7]. Hence, it is possible to establish a relation between these classical

polynomials and the transmission coefficient of a periodic system, but only for those intervals on the  $k$ -axis where the condition  $|z| < 1$  is satisfied. Since this quantity depends only on the properties of the single period, the position and the width of these Chebyshev ranges are independent of the number  $N$  of periods. In particular, for  $N \rightarrow \infty$  we can recognize in the Chebyshev ranges the energy bands of the corresponding 1D crystal and in the other intervals the forbidden bands [8].

Using the expression (2) for the modulus of the transmission coefficient it is simple to find the conditions for perfect transmission (PT). We have two possibilities:  $r = 0$  and  $P_{N-1}(z) = 0$ . In the first case there is PT through the whole system because each component is transparent. This condition depends on the details of the single period. The other condition comes from the periodicity and does not appear in the single spectrum. When  $|z| < 1$  these windows correspond to the  $(N - 1)$  roots of the Chebyshev polynomial of the second kind  $U_{N-1}(z)$ , given by:

$$z = \cos\left(\frac{\pi j}{N}\right), \quad j = 1, \dots, N - 1. \quad (4)$$

We can see that, although the wave numbers of these transmission peaks depend on the structure of the single period, their number is independent of this structure. The modulus of the transmission coefficient of a system with  $N$  periods presents exactly  $(N - 1)$  peaks in each Chebyshev interval and outside these ranges there is no PT and  $t_N$  approaches zero when  $N$  increases, as one can see from the behaviour of the  $P_N(z)$  if  $|z| > 1$ . Moreover, as a consequence of properties of the Chebyshev polynomials, the transmission spectrum of the system with  $N$  periods has all the perfect windows of the system with a number of periods equal to a divisor of  $N$ .

The support of the Swiss National Science Foundation through grant No.20-37642.93 is gratefully acknowledged.

## References

- [1] D.W.L.Sprung et al., Am.J.Phys. **61**, 1118 (1993)
- [2] P.Erdős and R.C.Herndon, Adv.Phys. **31**, 65 (1982)
- [3] F.Abelès, Ann.de Physique **5**, 777 (1950)
- [4] D.J.Vezzetti and M.M.Cahay, J.Phys.D **19**, L53 (1986)
- [5] M.Abramowitz and I.A.Stegun, *Handbook of Mathematical Functions* (Dover, New York, 1965)
- [6] T.M.Kalotas and A.R.Lee, Eur.J.Phys. **12**, 275 (1991)
- [7] D.J.Griffiths and N.F.Taussig, Am.J.Phys. **60**, 883 (1992)
- [8] R. de L.Kronig and W.G.Penney, Proc.Roy.Soc. (London) **A130**, 499 (1931)

## Vorticity Formation in an Electrostatic Precipitator

Edgar A. Gerteisen <sup>b</sup>, W. Egli <sup>a</sup> and B. Eliasson <sup>a</sup>

<sup>a</sup> ABB Corporate Research, CH-5405 Baden-Dättwil

<sup>b</sup> CSCS, Centro Svizzero di Calcolo Scientifico, Via Cantonale, CH-6928 Manno

A geometry bounded by two plane plates and with corona wires in the center plane is considered. At conditions with low gas velocity and high electrical current (high electrohydrodynamic number) vortices form between the wires and the plates. They are generated by the volume force resulting from the electric field multiplied by the space charge density. The time evolution is compared between a numerical finite volume Euler method and an integral approximation. For typical arrangements the time constant is of the order of 0.1s.

An electrostatic precipitator (ESP) consists of several rectangular channels. The polluted gas flows through these channels and the electric forces move the dust particles to the plates. Some of the important physical properties are the electric field, the space charge, the flow velocity field and the particles. The numerical simulation of the ESP-behavior is challenging because of the multi-disciplinary nature of the problem, where knowledge of specialists in different fields of physical modeling has to be combined. A data base concept [1] is used for enabling an efficient interaction of programs which have been developed independently by the various researchers.

The two-dimensional geometry considered consists of two grounded plates with high voltage electrodes in the symmetry plane (Fig. 1). In order to evaluate the time-constant for the formation of vortices,

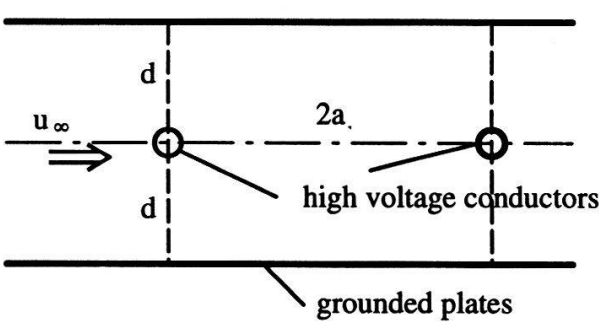


Fig. 1: Definition of the considered plane two plate geometry with conductors

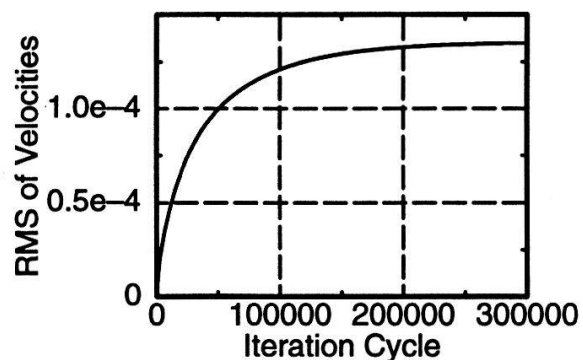


Fig. 2: RMS of velocity for the formation of vortices in a fluid cell configuration:  
 $u_{\infty} = 0$

an integral estimation of the equilibrium between electrostatic volume forces and momentum in the flowfield is considered. The electric force density is given by  $\varrho_i E$ , where  $\varrho_i$  and  $E$  define the space charge density and electric field respectively. Accordingly, the momentum equation for mean value quantities in a control volume  $a \cdot d \cdot 1$  reads:

$$\varrho u^2 d = d a \varrho_i E \quad \Rightarrow \quad u = \sqrt{a \frac{\varrho_i}{\varrho} E} = \sqrt{\frac{a \varrho_i}{d \varrho} U}$$

Applying the mean volume force to the control volume defines an acceleration  $b = \varrho_i E / \varrho$ , which leads to a time-constant for the transfer of applied electrical energy into mechanical energy:

$$\tau = \sqrt{\frac{ad}{U \varrho_i}} = \sqrt{\frac{a}{E \varrho_i}} = \frac{ad}{U} \sqrt{\frac{\varrho}{\varepsilon_0}},$$

where the space charge is estimated by  $\varrho_i = U \varepsilon_0 / (ad)$  [4]. Together with typical parameters for an ESP

( $U=50\text{kV}$ ,  $d=0.15\text{m}$ ,  $a=d$ ) the estimated values for the time-constant and mean velocity are:

$$\tau = 0.15 \text{ sec} , \quad u = 1 \text{ m/s} .$$

The estimated value for the time-constant is in good agreement (300 000 cycles correspond to 0.5 sec) with the gasdynamic model, whereas the root mean square of the velocities (normalized by the speed of sound) differs remarkably. The time for the formation of rotation is assumed to be independent of  $u_\infty$ , i.e. the magnitude of the incoming flow.

The source-terms for momentum and energy in the fluid equations, i.e. the forces that produce vortices, depend on the electric field and the space charge. The potential together with the space charge is solved using the ASTRID [2] system, which is part of the already mentioned PE<sup>2</sup>AR environment [1]. More recently the method for calculating the charge density distribution [3] and flow simulation modules have been implemented into the environment. Two different models are applied to solve the fluid equations together with the electrical forces. The steady state solution of the compressible Euler equations are calculated in a time-accurate iteration process (Fig. 2), whereas in an incompressible model the same numerical scheme is applied by using a pseudo-time relaxation [4,5]. The large number of iteration steps (Fig.2) reflects the physical stiffness, i.e. the physical time constant differs much from the time step limit imposed by the explicit method. Numerical problems are reported by different researchers for gasflows at low Mach-number. Incompressible models are more efficient, if they are able to solve the physical problem adequately. However, the structure of

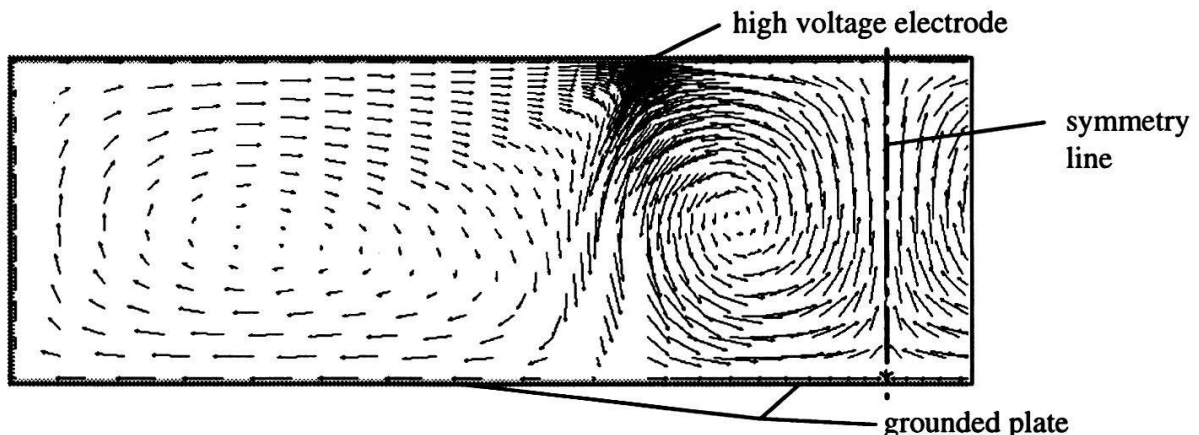


**Fig. 3:** Counter-rotating vortices generated by the electric field forces (ionic wind) in a closed cell filled with fluid

vortices computed with the incompressible method (Fig. 3) differ from that which has been received by solving the gasdynamic equations.

## References

- [ 1 ] R. Gruber, PE<sup>2</sup>AR: Program Environments for Engineering Applications and Research, CSCS-TR-94-06
- [ 2 ] E. Bonomi et al., Astrid: A Programming Environment for Scientific Applications on Parallel Vector Computers; Scientific Computing on Supercomputers II, Ed. J.T. Devreese and P.E. Van Camp, Plenum Press, New York 1990
- [ 3 ] W. Egli et al., Computation of the Charge Density Distribution in a 3D Electric field, Proceedings of the 6th joint EPS-APS International Conference on Physics Computing, PC'94, Lugano 1994
- [ 4 ] R.S. Sigmund, M. Goldmann, Corona Discharge Physics and Applications, Electric Breakdown and Discharge, Ed. E.E. Kunhardt, L.H. Luessen, Plenum Press, New-York, 1983
- [ 5 ] A.J. Chorin, A numerical method for solving incompressible viscous flow problems, *J. Comp. Phys.* 2, 12-26, 1967
- [ 6 ] A. Rizzi and Lars-Erik Eriksson, Computation of inviscid incompressible flow with rotation, *J. Fluid Mech.* (1985), vol 153, pp.275-312

## MHD ACTIVITY DURING H-MODE DISCHARGES ON THE TCV TOKAMAK.

A.HIRT, B.P.DUVAL, J.-M. MORET, A.POCHELON, G.TONETTI, H.WEISEN.  
Centre de Recherches en Physique des Plasmas, Av. des bains 21 , CH1007 - Lausanne

Ohmic H-mode has been regularly obtained on the TCV tokamak. This paper describes the change in magnetic activity occurring at the transition, the coherent activity during H-mode, a brief description of the dithering phase, and the activity associated with large and grassy ELMs.

**Introduction:** The H-mode [1] is a good candidate for the operating regime of future fusion experiments due to the associated enhanced energy confinement. There is still, however, no consensus about the physics governing the transition.

Edge Localized Mode (ELMs) are disruptive events occurring during the H-mode which cause a loss of particles at the plasma edge. They generally result in a lower particle confinement for the working gas and impurities and, in general, a lower energy confinement [2]. ELMs can occur in plasmas with widely different equilibrium parameters, leading to a separation into different ELM types [3]. Again, many of the physical processes resulting in ELMs are not understood, although many possible explanations have been proposed.

In this paper, we describe the L-H transition as observed by the MHD (Magneto-HydroDynamics) diagnostic of TCV, then summarise the coherent magnetic activity occurring during the H-mode and, finally, analyse the dithering and ELM phases. The typical values of the plasma parameters for these shots are: safety factor  $q_{95} = 2.2-2.7$ , elongation  $\kappa = 1.3-1.8$ , triangularity  $\delta = 0.3-0.8$ , toroidal field  $B_{\text{tor}} = 1.4\text{T}$  and plasma current  $I_p = 240-600\text{ kA}$ .

**The L-H transition:** The L-H transition is primarily seen by the MHD diagnostic as a 20 dB drop in low frequency ( $5\text{ kHz} < f < 30\text{ kHz}$ ) turbulence occurring on a timescale of  $100\text{ }\mu\text{s}$ . This change is generally seen on all the magnetic probes with a spatial repartition depending on the plasma configuration. On some double null (DND-U) discharges, the turbulence level in the immediate vicinity of the divertor legs remains unchanged (see *fig.1*) at the transition suggesting that a line-tying phenomenon [4] may contribute to the measured decrease in turbulence.

Mirnov activity, which has a typical poloidal and toroidal mode number  $m \geq 2$ ,  $n = 1$  in typical TCV L-mode discharges, has been observed to decrease and sometimes disappear at the transition. This change is observed even on probes where virtually no drop in turbulence is visible, suggesting a different physical reason for the change in coherent magnetic activity, a current profile modification during the H-mode being a potential mechanism.

**Coherent activity during H-mode:** When  $m \geq 2$ ,  $n = 1$  mode is still observed during H-mode, it approximately maintains its pre-transition frequency ( $5\text{ kHz}$ ) with a significantly lower amplitude. This mode is often observed as fishbone-like bursts synchronised with the sawtooth crash, with a greater amplitude on the low field side.

A higher frequency ( $15\text{ kHz} < f < 40\text{ kHz}$ ) coherent mode is also observed during the ELM-free H-mode, often with a double-frequency harmonic and simultaneously with a 10% increase in the divertor zone  $D_{\alpha}$  intensity.

**Dithering phase and ELMs:** When the conditions required for transition to the H-mode are only marginal, the plasma oscillates between L- and H-mode. On TCV, this dithering phase is characterised by repeated ( $f = 1-3\text{ kHz}$ ) peaks in the  $D_{\alpha}$  intensity, sometimes irregular. A burst of turbulent magnetic activity is detected during the  $D_{\alpha}$

intensity rise preceded by a growing coherent magnetic precursor ( $f=50-60$  kHz) typically starting 0.3 ms before the burst.

Large ELMs appear as strong bursts of MHD activity with a 100ms duration with a typical intensity of 200 T/s for a magnetic probe at a distance of 0.1 m from the plasma last closed flux surface. Their spectrum is characterised by wideband turbulence (up to 125 kHz, the limit of our instrumentation) together with some spatial coherence. The dominant  $m=1, n=0$  mode (i.e. an upwards movement of the plasma column) occurs together with a less intense  $m=2,3$  mode. The magnetic activity is followed by a  $D_\alpha$  intensity peak with a rise time lower than 0.1ms and a typical duration of 1ms. No quasi-coherent magnetic precursors before the large ELMs were seen, although high frequency ( $f > 80$  kHz) turbulence drop immediately after the ELM was observed. For the same plasma parameters, some discharges that exhibits large ELMs after a fresh boronisation remain ELM-free when the boronisation is worn [2]. Large ELMs thus tend to disappear with higher ohmic heating power, a behaviour typical of type III ELMs [4].

Grassy ELMs are visible on the MHD diagnostic as repetitive bursts of activity localised near the X points, with an amplitude of 50-100 T/s increasing with the plasma line averaged density  $n_e$ . They have a repetition frequency of  $300$  Hz  $< f < 5$  kHz, and tend to become stochastic at high density ( $n_e > 10^{20} \text{ m}^{-3}$ ). Grassy ELMs do not degrade the energy confinement, and were present during the discharge showing the highest confinement time to date (90 ms). Grassy ELMs never appear immediately after a L-H transition, and have always been observed at a line averaged density higher than  $4.9 \cdot 10^{19} \text{ m}^{-3}$ .

**Conclusion:** These results show that the MHD activity during H-mode on TCV is similar to other tokamaks. One discrepancy is that a coherent magnetic precursors before the large ELMs was not observed. In the future, enhanced MHD and soft-X diagnostics will make more quantitative results possible.

**Acknowledgments:** This work was partly supported by the Swiss National Science Foundation.

#### References:

- [1] ASDEX Team. Nucl. Fusion **29**, 3 (1989).
- [2] M.J.Dutch, F.Hofmann *et al.*, submit. to Nucl. Fusion, sept. 1994.
- [3] DIII-D team. Proc. of the 13th IAEA Conf., Washington (1990).
- [4] N. Ohyabu *et al.*, Nucl. Fusion **29**, 3 (1989).

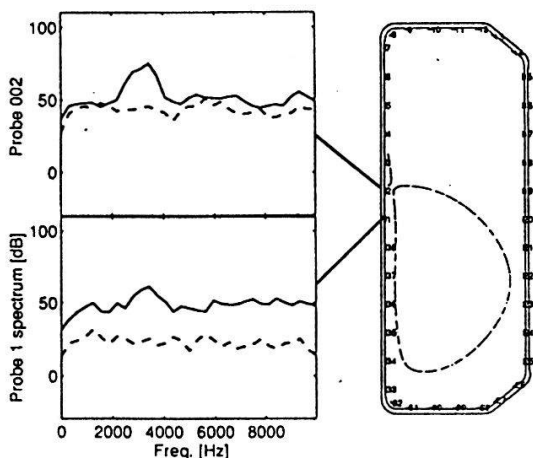


**Fig.1.** The two power spectra (continuous: before the L-H transition, dashed: after the transition) show that turbulence decreases on probe 1, but not on probe 2 (in the divertor leg impact zone), where only the coherent activity disappears (see text). The last closed flux surface is shown on the right side.

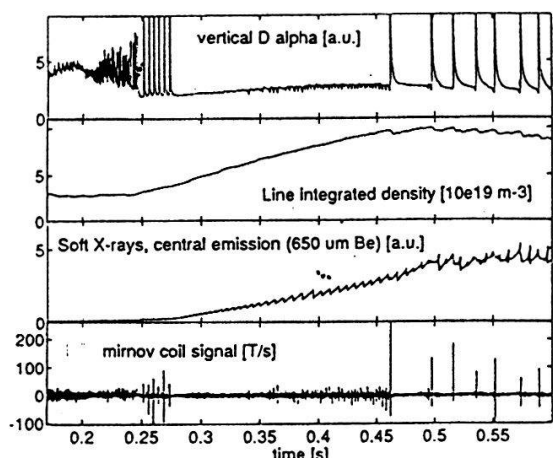


**Fig.2.** The beginning of a typical ohmic H-mode on TCV. The dithering phase ( $0.2s < t < 0.25s$ ) is followed by 6 large ELMs. After a short ( $0.28s < t < 0.34s$ ) quiescent phase, grassy ELMs appear. Finally ( $t > 0.34s$ ) we see repetitive large ELMs (note the behaviour of density).

## Characterization of high density arrays of quantum wires by photoluminescence and TEM

J. Robadey, U. Marti, F. Filipowitz, T. Hessler, D. Martin, F. Morier-Genoud,  
P. C. Silva, Y. Magnenat, and F. K. Reinhart

*Institute of Micro- and Optoelectronics, EPFL, CH-1015 Lausanne, Switzerland*

P.-H. Jouneau and F. Bobard

*Center for Electron Microscopy, EPFL, CH-1015 Lausanne, Switzerland*

The photoluminescence of high density GaAs and InGaAs arrays of quantum wires grown on non-planar substrates has been analyzed. These structures show a photoluminescence efficiency equal to that of a planar control quantum well. The full width at half maximum of the ground state transition is as small as 6 meV at 5 K. In the photoluminescence spectra, we observe a 1D level splitting of 12 meV due to the lateral confinement. This is in good agreement with model calculations based on transmission electron microscopy structural data. At increased excitation density, we observe a strong band filling. A photoluminescence analysis of InGaAs quantum wires grown at different temperatures shows a strong In desorption during the growth process at a temperature of 560°C or higher.

The interest on quantum wires (QWR) has increased over the past few years [1,2]. The strong quantization of electron and hole states due to lateral confinement leads to a density of states with a narrower energy distribution, compared to that of a quantum well, and is of great interest for studies and applications of QWR. Important progress in nanotechnology now permits the production of QWR with width down to 10 nm. However the fabrication of high quality QWR remains difficult. We use photoluminescence (PL) and transmission electron microscopy (TEM) to assess the quality of the wires. Results of PL measurements and TEM observations are also used to optimize the fabrication process.

Our samples are reproducibly fabricated by a combination of deep UV holographic lithography and molecular beam epitaxial (MBE) growth on periodic non-planar substrates [3]. Arrays of GaAs/AlGaAs QWR and InGaAs/GaAs QWR are grown at the bottom of V-grooves. They have a crescent shape with typical lateral size in the 20 nm range (Fig. 1). The vertical thickness is maximal in the center of the wire and decreases continuously towards the sides. By assuming that the lateral confinement potential at a lateral position of the QWR is equal to the lowest energy level of a quantum well of equal thickness, we can calculate the electron and hole energy levels due to the lateral potential. These calculated energy levels, deduced from the structural information of TEM observations, are in good agreement with PL measurements.

InGaAs QWR arrays with identical processing parameters except for the substrate temperature during growth process were analyzed. The samples were grown at substrate temperatures of 540°C, 560°C, and 580°C. The In flux in the MBE chamber was set to give an In concentration of 18% in control planar quantum wells grown at 540°C. TEM micrographs illustrate a strong desorption of In at 580°C (Fig. 1). PL measurements at 86 K on three comparable samples yield a shift of the InGaAs QWR peaks towards bulk GaAs for the high growth temperatures: the peaks

corresponding to the ground excitonic transition are located at 1377 meV, 1424 meV, and 1477 meV for substrate temperatures of 540°C, 560°C, and 580°C respectively.

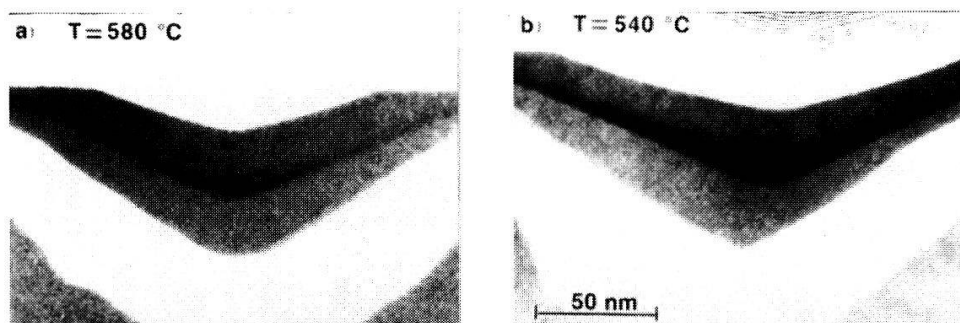


FIG. 1. TEM picture of InGaAs/GaAs QWR grown at (a) 580°C and (b) 540°C. The light gray area represents AlAs/GaAs superlattices, the medium gray GaAs and the black the InGaAs QWR. A strong In desorption during the growth process is observed for the sample grown at 580°C.

Figure 2 shows PL spectra for different excitation densities for another sample grown at 560°C. The two first levels  $n_y=1$  and  $n_y=2$  resulting of the lateral confinement are clearly seen at 1438 meV and 1450 meV respectively. The splitting between the second and the fundamental excitonic transition is therefore equal to 12 meV. A saturation of the first level versus the second one takes place near  $25 \text{ mW/cm}^2$ , and corresponds to the expected 1D behavior of QWR. The PL efficiency is as good as for planar control quantum well structures.

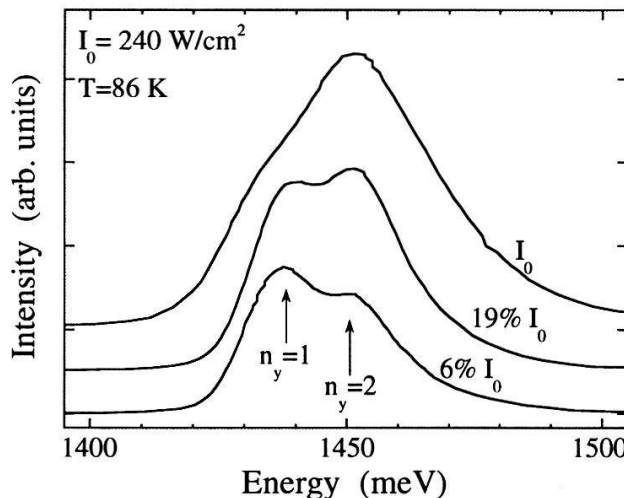


FIG. 2. PL spectra of a sample grown at 560°C for different excitation energies. A 1D level splitting of 12 meV due to lateral confinement is observed. A clear saturation of the first peak versus the second one occurs at the higher excitation densities. This is typical for structures with 1D quantum lateral confinement.

## Conclusion

We demonstrate the fabrication of high density QWR arrays with strong 1D lateral quantum properties observed by PL. TEM and PL permit precise characterization of the QWR arrays and the optimization of their fabrication process. Significantly, the PL efficiency was found to be equal to that of a control quantum well.

- [1] R. Cingolani and R. Rinaldi, *Rivista del Nuovo Cimento* **16**, 1 (1993).
- [2] E. Kapon, *Optoelectronics* **8**, 429 (1993).
- [3] U. Marti, M. Proctor, D. Martin, F. Morier-Genoud, B. Senior, F. K. Reinhart, *Microelectronic Engineering* **13**, 391 (1991).

## FABRICATION AND CHARACTERIZATION OF QUANTUM WIRES IN OPTICAL WAVEGUIDE STRUCTURES

F. Filipowitz, U. Marti, J. Robadey, D. Martin, F. Morier-Genoud, P.C. Silva, I. Magnenat, \*P. Ruterana, \*P.-H. Jouneau, \*F. Bobard, F.K. Reinhart

*Institut de micro- Optoélectronique, \*Institut interdépartemental de microscopie électronique, Ecole Polytechnique Fédérale de Lausanne, CH-1015 LAUSANNE*

**Abstract :** InGaAs Quantum wires are made by MBE growth on non-planar substrates. These new structures clearly show 1D quantum levels and are suitable for future device applications in waveguides. We demonstrate a waveguide photodetector that exhibits 1D level splitting.

Quantum well wires (QWW) are expected to exhibit larger electro-absorption and electro-refraction [1], enhanced optical non-linearities [2] and higher differential optical gain [3] compared to that of quantum well (QW) structures. Our GaAs and InGaAs QWW made by MBE growth on non-planar substrates [4] clearly show 1D quantized states [5]. The high degree of uniformity and good photoluminescence (PL) properties makes these QWW candidates for new device applications. Integration of the QWW in waveguides is the next step toward devices.

### QWW Fabrication :

V-groove QWW made by MBE growth on a non-planar substrate patterned by holographic lithography have several advantages for devices applications: holographic lithography is an inexpensive and rapid process to provide high package density (period  $\geq 90$  nm) over wide areas ( $> 2$  cm $^2$ ); fabrication of QWW by MBE growth on a non-planar substrate greatly reduces the density of non-radiative recombinations centers, if compared to classical QWW fabrication processes based on QW etching.

The lateral confinement of a GaAs QWW embedded in AlGaAs is a consequence of the higher growth rate on (n11) facets,  $n>1$ , compared to (100) facets. In our approach the lateral confinement is enhanced by growth interruption just after deposition of the GaAs. During this process, mass transport of Ga into the valley of the V-groove occurs and a crescent shape QWW is formed (cf. Figure 1). This new shape reduces the effective width of the lateral confinement potential to less than 20 nm. InGaAs QWW embedded in GaAs can also be grown by this method.

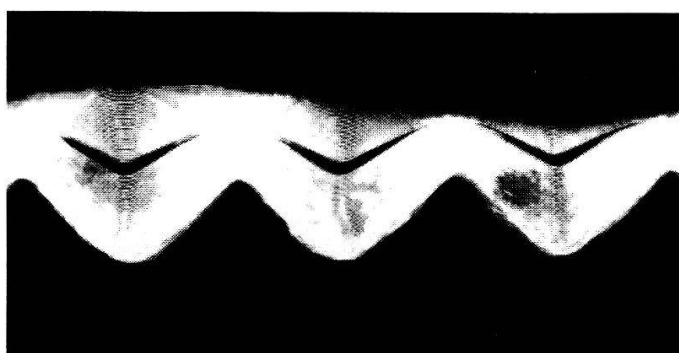


Figure 1: TEM photography of a GaAs (black) QWW embedded in an AlAs (white)/GaAs superlattice. The sawtooth profile at the bottom is the non-planar GaAs substrate. The distance between two adjacent wires is 200 nm. Rapid planarization is observed.

### Integration of QWW in optical waveguides :

The integration of GaAs QWW in waveguides poses the following problems: (1) during growth of most InAlGaAs compositions on non planar profiles, complete planarization occurs after about 150 nm of grown material, (2) regrowth on AlGaAs with more than 15% Al dramatically increases the defect density due to incomplete desorption of Al oxide before regrowth. To overcome this problem a waveguide core consisting of GaAs is grown (regrowth on GaAs is not problematic). The process sequence is as follow: (i) MBE growth of the lower waveguide cladding ( $Al_{0.33}Ga_{0.67}As$ ) and half of the waveguide core (GaAs), (ii) patterning of the core, (iii) MBE growth of InGaAs QWW, second part of the GaAs core and the upper cladding ( $Al_{0.33}Ga_{0.67}As$ ). The result of this process is shown in Figure 2. For applications the lower cladding is n-type doped, whereas the upper cladding is p-typed doped. The QWW and the waveguide core are nominally undoped.



Figure 2: SEM photography of InGaAs QWW in a waveguide. Distance between two adjacent wires is 180 nm

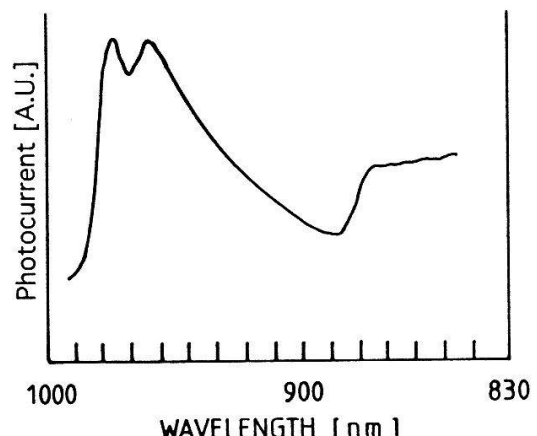


Figure 3: Photocurrent (300K) response of the InGaAs QWW waveguide detector

### Measurements :

First measurements were made on waveguides containing InGaAs QWW and a p-n junction. Transmission measurements show loss of  $12 \text{ cm}^{-1}$  (at  $1.15 \mu\text{m}$ ). Room temperature photocurrent measurements with a  $Ti:Al_2O_3$  laser emission coupled into the InGaAs QWW waveguide clearly show two well resolved 1D levels separated by 24 meV. These results are in good agreement with PL measurements [6]. The full linewidth at half maximum is 18 meV. This structure appears to be suitable for a future wavelength demultiplexer device.

### References :

- [1] D.A.B. Miller, D.S. Chemla, S. Schmitt-Rink, *Appl. Phys. Lett.* **52**, 2154 (1988)
- [2] S. Schmitt-Rink, D.A.B. Miller, D.S. Chemla, *Phys. Rev B* **35** 8113 (1987)
- [3] Y. Arakawa, A. Yariv, *IEEE J. Quantum Electron.* **22**, 1887 (1986)
- [4] U. Marti, M. Proctor, D. Martin, F. Morier-Genoud, B. Senior, F.K. Reinhart, *Microelectronic Engineering* **13**, 391 (1991)
- [5] R. Rinaldi, R. Cingolani, M. Ferrara, A. Maciel, J. Ryan, U. Marti, D. Martin, F. Morier-Genoud, F.K. Reinhart, E. Molinari, F. Rossi, L. Rota, P. Lugi, *Appl. Phys. Lett.* **64** (26), 3587 (1994)
- [6] J. Robadey, U. Marti, F. Filipowitz, T. Hessler, D. Martin, F. Morier-Genoud, P.C. Silva, I. Magnenat, P-H. Jouneau, F. Bobard, F.K. Reinhart, *Helv. Phys. Acta* (1994)

# SPIN DEPENDENCE IN SCATTERING OF 14 MEV ELECTRONS FROM LEAD NUCLEI

D. Conti, K. Bodek, H.K. Kayser\*, J. Lang, S. Navert, O. Naviliat, E. Reichert\*, J. Sromicki, K.-H. Steffens\*, M. Steigerwald\*, E. Stephan, J. Zejma  
 Institut für Teilchenphysik, ETH, 8093 Zürich, Switzerland  
 \* Institut für Physik, J. Gutenberg Universität, Postfach 3980, W-6500 Mainz, Germany

We studied polarization effects in the elastic scattering of 14 MeV electrons from lead nuclei. The left-right asymmetry was measured at two scattering angles as a function of the target thickness using a polarized ( $P \simeq 0.3$ ) monochromatic electron beam extracted after the first stage of the Mainz Microtron. The measured analyzing powers are in good agreement with Mott scattering theory. Effects of finite size of the lead nuclei are perceivable. The depolarization in thick scattering foils was measured for the first time for electrons in energy range nonaccessible with  $\beta$ -decay sources.

In order to calibrate the polarimeter of our experiment searching for time reversal violation in the  $\beta$ -decay of  ${}^8\text{Li}$  [1] we investigated the elastic scattering of electrons from lead nuclei. We report the first results of our study of the effective analyzing power for thick scattering targets. Due to multiple scattering effects the effective analyzing power is a decreasing function of the target thickness. No measurements of such depolarization effects in the energy range above 1 MeV have been done. The left-right asymmetry was measured as a function of the target thickness at two scattering angles simultaneously. The asymmetries were then extrapolated to the infinitely thin foils. Using the values of the beam polarization  $P$  measured at lower and higher energies, the analyzing power  $A$  of the elastic scattering at 14 MeV was extracted and compared to the theoretical predictions. Conversely, by assuming the theoretical analyzing power for Mott scattering [2], the beam polarization can be inferred from the extrapolated asymmetries.

The asymmetries were measured with two sets of triple coincidence telescopes placed left and right to the beam at  $138.7^\circ$  and  $159.4^\circ$  scattering angles. The beam polarization obtained from the Mott (100 keV) and the Møller (855 MeV) polarimeters of the Mainz accelerator was  $P = 0.33 \pm 0.02$ . The uncertainty quoted is a combined error of both methods. The targets were lead foils with thicknesses between  $17 \text{ mg/cm}^2$  and  $250 \text{ mg/cm}^2$ . The background was studied periodically in measurements with an empty target frame. The dead-time and background effects were found to be relatively small. The asymmetry  $\epsilon$  was calculated by using :

$$\epsilon = P \cdot A = \frac{\sqrt{(N_{R_u} N_{L_d})} - \sqrt{(N_{L_u} N_{R_d})}}{\sqrt{(N_{R_u} N_{L_d})} + \sqrt{(N_{L_u} N_{R_d})}} \quad (1)$$

where  $u, d$  refers to the polarization of the beam and  $L, R$  (left, right) refers to the position of the detectors with respect to the beam axis.

The measured asymmetry as a function of the target thickness is shown in Fig. 1. The decrease of the asymmetry  $\epsilon$  with increasing thick-

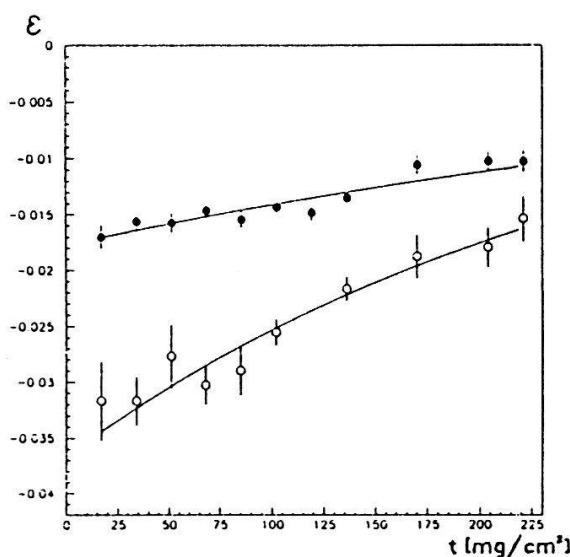


Figure 1: Asymmetry for  $138.7^\circ$  and  $159.4^\circ$  scattering angles as a function of the thickness of the target

ness  $t$  of the foil was parametrized using :

$$\epsilon = \epsilon_0 \cdot e^{-\alpha \cdot t} \quad (2)$$

where  $\alpha$  [ $\text{cm}^2/\text{mg}$ ] represents the depolarization parameter,  $t$  is the target thickness in  $\text{mg}/\text{cm}^2$  and  $\epsilon_0$  is the asymmetry extrapolated to infinitely thin foils. The resulting fit parameters are :

Angle	$\alpha$	$\epsilon_0$
$138.7 \pm 1^\circ$	0.0025(3)	-0.0179(6)
$159.4 \pm 1^\circ$	0.0032(5)	-0.0350(21)

Assuming the polarization of the electron beam measured by the polarimeters of the Mainz accelerator we extracted the analyzing powers  $A_0^{Exp.}$  from the extrapolated asymmetries. The table below shows the results of the interpolation of the theoretical data ( $A_0^P, A_0^E$  for point nucleus and extended nucleus calculations, respectively) compared to the analyzing powers determined in the experiment.

Angle	$A_0^P$	$A_0^E$	$A_0^{Exp.}$
$138.7 \pm 1^\circ$	-0.065(2)	-0.052(1)	-0.054(4)
$159.4 \pm 1^\circ$	-0.133(3)	-0.104(2)	-0.106(7)

The errors of the theoretical values reflect the uncertainties in the interpolation. The errors of the experimental analyzing powers take into account contributions from counting statistics as well as geometrical uncertainties, however they do not include a common normalization factor uncertainty of  $\pm 7\%$  arising from the measurements of the beam polarization. Our experimental results are in very good agreement with the extended nucleus calculations. However, we note that this conclusion relies to some extent on the measurement of the beam polarization.

By taking the quotient between the analyzing powers at the two angles the beam polarization can be eliminated. We obtain the results:

$$\begin{array}{ccc} \frac{A_0^E(138.7^\circ)}{A_0^E(159.4^\circ)} & \frac{A_0^P(138.7^\circ)}{A_0^P(159.4^\circ)} & \frac{A_0^{Exp.}(138.7^\circ)}{A_0^{Exp.}(159.4^\circ)} \\ 0.50(2) & 0.49(2) & 0.51(5) \end{array}$$

that confirm correct angular dependence of the calculated Mott analyzing power.

In conclusion, good agreement with the theory was found in this first measurement of the polarization effects in Mott scattering for highly relativistic electrons. The calculated values of the Mott analyzing power may be used with confidence to analyze the polarization of electrons with energies up to few tens of MeV. The measurements of depolarization effects for thick scattering targets are very valuable for the construction of electron polarimeters in this energy range as e.g. the one used in our experiments searching for violations of fundamental symmetries in weak interactions.

## References

- [1] M. Allet, W. Hajdas, J. Lang, H. Lüscher, R. Müller, O. Navillat-Cuncic, J. Sromicki, A. Converse, W. Haeberli, M. A. Miller and P. A. Quin, Phys. Rev. Lett. **68** (1992) 572
- [2] P. Uginčius, H. Überall, G. H. Rawitscher, Nuclear Physics A158 (1970) 418-432

## Muon Transfer Rates to Helium in $H_2 + He + Ar$ Gas Mixtures: a new Evaluation

C. Piller, O. Huot, R. Jacot-Guillarmod, F. Mulhauser, L.A. Schaller, L. Schellenberg, H. Schneuwly, S. Tresch, Y.-A. Thalmann and A. Werthmüller.

Institut de physique de l'Université, CH-1700 Fribourg, Switzerland

The first calculations of the muon transfer rate from muonic hydrogen atoms to helium predicted a very low value. They have been confirmed by a first experiment which yielded a rate  $\Lambda_{dHe} < 0.1 \cdot 10^8 s^{-1}$  [1] for the transfer from muonic deuterium. In 1981, another mechanism was proposed yielding a rate which should be more than an order of magnitude greater [2]. Soon after, this rate was also confirmed in triple mixtures  $H_2 + He + Xe$  by Bystritsky et al. [3].

At that time, three different values for the reduced transfer rate to argon were given in the literature:  $1.4 \cdot 10^{11} s^{-1}$ ,  $3.6 \cdot 10^{11} s^{-1}$  and  $9.8 \cdot 10^{11} s^{-1}$ . Planning to measure the transfer rate to helium in triple mixtures  $H_2 + He + Ar$ , we measured at first the transfer rate to argon in four binary mixtures  $H_2 + Ar$  at pressures of 9.6, 14.9, 100 and 140 bar and obtained values between  $1.41 \cdot 10^{11} s^{-1}$  and  $1.48 \cdot 10^{11} s^{-1}$  [4,5]. In particular at low pressures, no deviation of the time structure of the muonic argon X-rays from a single exponential was observed [4]. With a mean value of  $\Lambda_{pAr} = (1.44 \pm 0.04) \cdot 10^{11} s^{-1}$ , the mean value of the transfer rate to helium deduced from the triple mixtures was  $\Lambda_{pHe} = (0.88 \pm 0.09) \cdot 10^8 s^{-1}$ , in disagreement with the value obtained by Bystritsky et al. [3].

With a new experiment using a triple mixture  $H_2 + He + CH_4$ , we planned to remeasure the transfer rate to helium. Thus, we determined at first the transfer rate to carbon in binary mixtures  $H_2 + CH_4$  at pressures of 10, 15 and 40 bar with a relative  $CH_4$  concentration of 0.175%. As illustrated by Fig. 1, the time distributions of the muonic carbon X-rays strongly deviate from the expected single exponential structure. The analysis revealed, that the time extention of the deviation is strongly related to the total pressure [6]. The lower the pressure the higher is the rise time, which indicates that one has to do with a thermalization process.

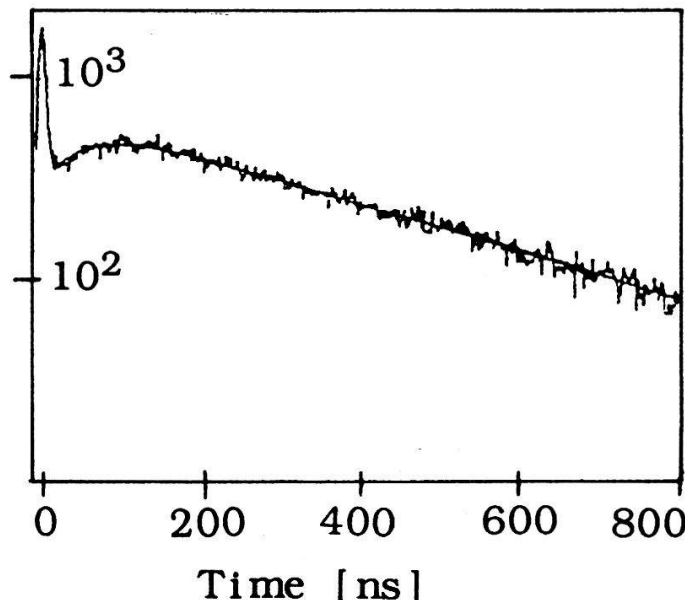


Figure 1 : Time spectrum of muonic carbon 2p-1s transition in  $H_2 + 0.18\% CH_4$

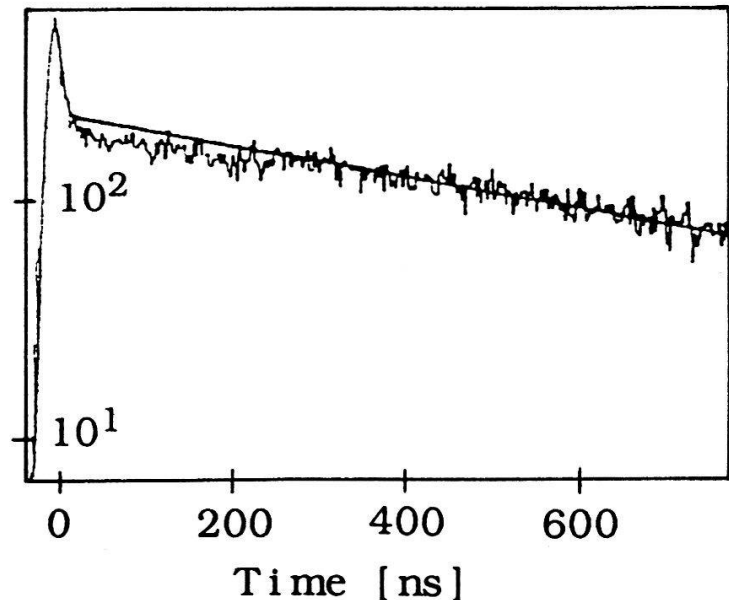


Figure 2 : Time spectrum of muonic argon 2p-1s transition in  $H_2 + 0.28\% Ar$  fitted with a single exponential for  $t > 300$  ns

The muon transfer rate from thermalized muonic hydrogen atoms in the ground state to carbon has been determined from the time constant of the exponential function fitting the upper part (e.g.  $t > 200$  ns at 15 bar) of the time distributions of the muonic carbon K-X-rays measured in the binary mixtures. From the three values measured at the three different pressures, one obtains a mean value (reduced to the atomic density of liquid hydrogen) of

$$\Lambda_{pC} = (0.95 \pm 0.05) \cdot 10^{11} \text{ s}^{-1}$$

In the triple mixture  $H_2 + 50\%He + 0.179\%CH_4$  at 15 bar, the rise time of the time distribution of the muonic carbon X-rays is much shorter than in the binary mixture at the same pressure. The thermalization of the  $\mu p$  atoms in collisions with helium atoms is faster than with hydrogen molecules. From the upper part of the time distribution ( $t > 200$  ns), one measures a decay rate,  $\lambda_{mes}$ , of the muonic hydrogen atoms in the triple mixture. By using the value for the transfer rate to carbon determined in the binary mixtures, one can calculate the transfer rate to helium from the measured decay rate. In the triple mixture employed, the measured decay rate was determined by more than 80% by the muon transfer to carbon. In the present case, the uncertainty of the transfer rate to carbon was too large and the statistics accumulated too low to determine with precision the transfer rate to helium. The upper limit of

$$\Lambda_{pHe} < 0.6 \cdot 10^8 \text{ s}^{-1}$$

agrees with the theoretical prediction as well as with the value of Bystritsky et al. [3]. It disagrees however with the transfer rate deduced from the measurements performed in  $H_2 + He + Ar$  mixtures [4].

Although our preceding measurements of the transfer rate to argon yielded consistent rates [4,5], we decided to remeasure this rate in a binary mixture  $H_2 + 0.28\%Ar$  at 15 bar by accumulating a higher statistics. In addition, care was taken to reduce further the background. The measured, background subtracted time distribution of the muonic  $K_\alpha$  argon X-rays is shown in Fig. 2. By fitting only the upper part ( $t > 300$  ns) with a single exponential function, the extrapolation to smaller times reveals a deviation which was not observed in our previous measurements. The transfer rate to argon deduced from this fit is  $\Lambda_{pAr} = (1.6 \pm 0.1) \cdot 10^{11} \text{ s}^{-1}$ , in disagreement with all former transfer rates.

If one calculates with this new transfer rate to argon the transfer rate to helium from the data of the  $H_2 + He + Ar$  mixtures [4], one obtains a new mean value of  $\Lambda_{pHe} = (0.5 \pm 0.1) \cdot 10^8 \text{ s}^{-1}$ . This value agrees with the upper limit deduced from the  $H_2 + He + CH_4$  mixture, and is only slightly but significantly higher than the value of  $\Lambda_{pHe} = (0.36 \pm 0.10) \cdot 10^8 \text{ s}^{-1}$  measured by Bystritsky et al. [3].

Although it is satisfactory to have now agreement between these three different measurements of the transfer rate from  $\mu p$  atoms to helium, it remains difficult to accept four different and incompatible transfer rates to argon. In addition, we have no explanation yet why a structure appears in the argon time distribution which was not visible in preceding measurements performed under quite similar conditions [4]. Thus, the present results with argon can only be regarded as preliminary and will have to be confirmed by additional measurements.

1. A. Bertin et al., Nuovo Cimento Lett 18 (1977) 381
2. Yu.A. Aristov et al., Sov. J. Nucl. Phys. 33 (1981) 564
3. V.M. Bystritsky et al., Sov. Phys. JETP 57 (1983) 728
4. R. Jacot-Guillarmod et al., Phys. Rev. A 38 (1988) 3106
5. F. Bienz et al., J. Phys. B: At. Mol. Opt. Phys. 21 (1988) 2725
6. L. Schellenberg et al., Proc. Int. Workshop on Muonic Atoms and Molecules, Ascona 1992, ed. by L.A. Schaller and C. Petitjean, Birkhäuserverlag Basel 1993, p. 187

## Muon Capture Ratios in Ar + Ne Mixtures

Y.-A. Thalmann, O. Huot, R. Jacot-Guillarmod, F. Mulhauser, C. Piller, L.A. Schaller, L. Schellenberg, H. Schneuwly, S. Tresch and A. Werthmüller

Institut de physique de l'Université, CH-1700 Fribourg, Switzerland

By analyzing the yields of the muonic X-rays of the Lyman series in  $Z_1 + Z_2$  mixtures, one determines atomic muon capture ratios. Our repeatedly measured capture ratios in 1:1 mixtures of Ar + Ne agree all with each other but disagree with the ratios measured by other authors.

The first theoretical work on atomic capture of negative "mesotrons" was published in 1947 by Fermi and Teller [1]. This famous article predicted a probability of capture approximately proportional to charge number  $Z$  of the atom. But the results of the first measurements performed in 1963 disagreed with the predicted values. Since then, more complex models alternated with new and more precise experiments, but no model is really satisfactory yet [2]. The principal reason is that experimental data are not compatible with each other, as shown in the Table for gaseous mixtures Ar + Ne.

Capture ratios have been determined in a lot of solid compounds. Measurements with pions and muons have shown that the chemical bond plays a decisive role in the capture mechanism [2]. Therefore, we decided to focus our study to noble gases in order to avoid molecular effects.

Experiments of capture ratios obey to a simple diagram : muons are stopped in a target and form excited muonic atoms, which emit X-rays while deexciting. X-rays energies are characteristic of the nuclei and the transition. All stopped muons end their cascade in the ground state. Because they make one and only one transition to the 1s state, the sum of the intensities of the muonic Lyman series of an element indicates the number of muons captured by this element. If one assumes that the capture is proportional to the number of atoms  $Z$  in the target, the per-atom muon capture ratio is determined by dividing the intensities of the Lyman series of the elements taking into account the stoichiometrical balance. For a 1:1 mixture of argon and neon, this ratio simply is :

$$A(\text{Ar,Ne}) = \frac{\sum_n I_{\text{Ar}}(n-1)}{\sum_n I_{\text{Ne}}(n-1)}$$

Because the spatial muon stop distribution inside the gas target is not known with precision, the absorption of the target walls has been studied in a separate experiment. The efficiency of the detection system and the transmission of the target walls, which have been measured by using a set of radioactive sources of known relative intensities, have been checked by comparing the muonic intensities of the Balmer series in argon with the prediction of a muon cascade calculation which reproduces the measured intensities of the Lyman series [3]. In addition, a plastic scintillator was placed before the target and a condition of coincidence was set in order to reduce background events on the semi-conductor detector.

We have performed three measurements, one in 1988 and two others in 1993, in 1:1 mixtures of Ar + Ne at room temperature and at a pressure of 15 bar. Two independent semiconductor detectors were used. All results agree well with each other, the mean value is [4] :

$$A(\text{Ar,Ne}) = 1.26(5).$$

Because the measurements of the other groups were different in pressure and muon momentum, we have investigated the influence of the two parameters in 1994 (see details in the Table). We have changed the momentum and the pressure. The capture ratios remained the same in the limits of the error, and no systematic trend was found.

Authors, year	$P_\mu$ [MeV/c]	Pressure [bar]	$A(\text{Ar,Ne})$
Budyashov et al., 1967 [5]	127	60	1.64(6)
Pfeiffer et al., 1975 [6]	?	180	1.11(14)
Hutson et al., 1980 [7]	80	10	1.41(7)
Ehrhart et al., 1983 [8]	115	50	1.01(3)
Thalmann et al., 1993 [4]	38	15	1.26(5)*
This work	39	15	1.29(5)
	75	15	1.28(6)
	30	5	1.30(6)

\* Mean value of three measurements in 88 and 93.

Table : Measured values for muon capture ratio  $A(\text{Ar,Ne})$  in gaseous mixture 1:1.

We are not able to explain yet why these muon capture ratios are so different. On the other hand, our value is the only one which has been reproduced under different experimental conditions.

### References :

- [1] E. Fermi and E. Teller, Phys. Rev. **72**, 399 (1947).
- [2] H. Schneuwly, Hyperf. Int. **82**, 133 (1993).
- [3] Y.A. Thalmann, diploma work, Institut de Physique de l'Université, Fribourg, 1993 (unpublished).
- [4] Y.A. Thalmann et al., Helv. Phys. Acta **66**, 895 (1993).
- [5] Yu. Budyashov et al., Sov. J. Nucl. Phys. **5**, 589 (1967).
- [6] H.-J. Pfeiffer et al., Nuclear Physics **A254**, 433 (1975).
- [7] R.L. Hutson et al., Phys. Lett. **A76**, 226 (1980).
- [8] P. Ehrhart et al., Z. Physik **A311**, 259 (1983).

## Muon Transfer Rates from Thermalized $\mu p$ and $\mu d$ Atoms to Oxygen

A. Werthmüller, O. Huot, R. Jacot-Guillarmod, F. Mulhauser, C. Piller, L.A. Schaller, L. Schellenberg, H. Schneuwly, Y.-A. Thalmann and S. Tresch

Institut de physique de l'Université, 1700 Fribourg, Switzerland

**Abstract:** Negative muons are trapped in  $H_2$  or  $D_2$  gaseous mixtures containing small amounts of  $CO_2$  and  $O_2$ . The muonic hydrogen atom may transfer its muon to other elements during collisions with other atoms. The resulting muonic cascade and the time distribution of the characteristic X-rays can be used to determine transfer rates from thermalized  $\mu p$  and  $\mu d$  atoms to oxygen. This analysis may clarify whether or not the transfer process is influenced by chemical bonds.

In gaseous mixtures of hydrogen containing small concentrations of an element  $Z$ , the extinction of  $\mu p$ -atoms is due to: muon decay, formation of  $pp\mu$ -molecules or transfer of the muon to other elements. The total extinction rate can then be written as:

$$\lambda = \lambda_0 + \lambda_{pp\mu} + \lambda_d + \lambda_Z$$

If the measurements are performed using natural hydrogen, one must also take into account the transfer to deuterium ( $\lambda_d$ ). The rate  $\lambda_Z$  also includes the transfer of a muon to different elements of a molecule, such as for  $CO_2$ . Knowing the transfer rate to carbon [1], it is possible to extract the rate to oxygen using the following relation:

$$\lambda_{CO_2} = \lambda_C + 2\lambda_O$$

To compare transfer rates measured under different experimental conditions, one usually normalizes them to the atomic density of liquid hydrogen ( $\rho = 4.25 \cdot 10^{22} \text{ cm}^{-3}$ ). Normalized (or reduced) rates  $\Lambda_Z$  for oxygen are presented in Tables 1 and 2.

The time distribution of the muonic oxygen transition  $2p-1s$  is given in Figure 1. The prompt peak represents direct muon capture by oxygen. At the same time it defines the moment at which the muon is stopped in the mixture. The delayed part of the spectra can be divided into two parts. While the first part has a rather complex structure, the second part is well described by a simple exponential function.

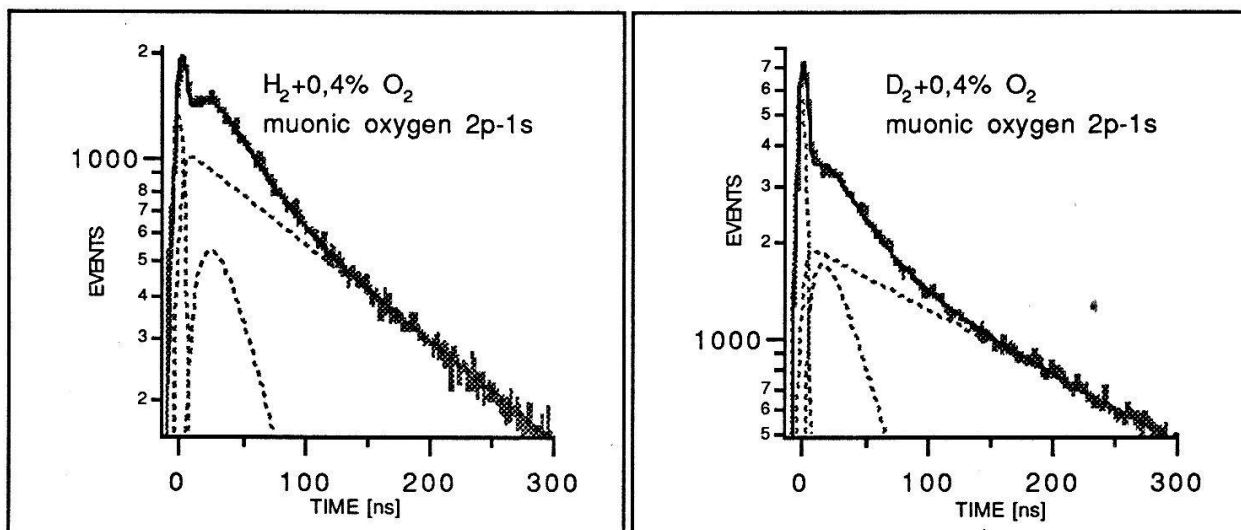


Figure 1

Recent work on the cascade of the muonic hydrogen atom [2] has shown that a significant fraction of these atoms will have epithermal energies when reaching the ground state. Monte Carlo simulations of a gaseous hydrogen mixture at 15 bar were performed to study the thermalization process [3]. According to the results, one can hypothesis that, 200 ns after a muon stop, the main part of the  $\mu$ -atoms will be thermalized. Therefore, to determine the transfer rate from thermalized muonic hydrogen atoms only the second part of the measured time distribution is analysed.

The results of such an analysis are presented in Table 1 for three different types of hydrogen mixtures at a pressure of approximately 15 bar and at room temperature. One can see that the extracted transfer rates to oxygen are in good agreement. This fact testifies that the transfer process from thermalized  $\mu$ -atoms in the ground state to oxygen is not dependent on chemical structure, at least for the investigated molecules. The relatively large error of the mean lifetime in the  $\text{CO}_2$  mixture comes from poor statistics.

gas mixture	Ref.	mean lifetime of $\mu$ p	$\Lambda_{\mu Z}$ [ $\cdot 10^{11} \text{ s}^{-1}$ ]	$\Lambda_{\mu O}$ [ $\cdot 10^{11} \text{ s}^{-1}$ ]
$\text{H}_2 + 0,4\% \text{ O}_2$	this work	$156 \pm 3 \text{ ns}$	—	$0,86 \pm 0,03$
$\text{H}_2 + 0,2\% \text{ CO}_2$	this work	$187 \pm 20 \text{ ns}$	$0,95 \pm 0,05$	$0,92 \pm 0,12$
$\text{H}_2 + 0,4\% \text{ SO}_2$	[4]	$107 \pm 2 \text{ ns}$	$0,89 \pm 0,09$	$0,83 \pm 0,08$

Table 1: The experimental results of the transfer measurements in hydrogen. The reduced transfer rate for carbon is taken from Reference [1].

At this time a similar analysis can not be performed for deuterium because the transfer rate from deuterium to carbon has not been measured. Therefore it is only possible to make a comparison between the results of  $\text{SO}_2$  and  $\text{O}_2$ . Assuming that the transfer rates from thermalized muonic deuterium atoms are also independent of chemical bonds the transfer rate to oxygen can be used to calculate the value for carbon.

gas mixture	Ref.	mean lifetime of $\mu d$	$\Lambda_{dZ}$ [ $\cdot 10^{11} \text{ s}^{-1}$ ]	$\Lambda_{dO}$ [ $\cdot 10^{11} \text{ s}^{-1}$ ]
$\text{D}_2 + 0,4\% \text{ O}_2$	this work	$211 \pm 5 \text{ ns}$	—	$0,62 \pm 0,02$
$\text{D}_2 + 0,4\% \text{ SO}_2$	[4]	$119 \pm 4 \text{ ns}$	1,10	0,55
$\text{D}_2 + 0,2\% \text{ CO}_2$	this work	$254 \pm 20 \text{ ns}$	$0,7 \pm 0,2$	0,62

Table 2: The experimental results of the transfer measurements in deuterium. For the  $\text{CO}_2$  results one shall refer to the text.

- [1] Huot et al, PSI News Letter 1993
- [2] V.E. Markushin, Phys. Rev. A50 (1994) 1137
- [3] A. Adamczak, private communication
- [4] F. Mulhauser and H. Schneuwly, J. Phys. B: At. Mol. Opt. Phys. 26 (1993) 4307–4332